The 8 May 2009 Superderecho: Analysis of a Real-Time Explicit Convective Forecast

MORRIS L. WEISMAN AND CLARK EVANS*

National Center for Atmospheric Research,+ Boulder, Colorado

LANCE BOSART

University at Albany, State University of New York, Albany, New York

(Manuscript received 21 March 2012, in final form 20 November 2012)

ABSTRACT

Herein, an analysis of a 3-km explicit convective simulation of an unusually intense bow echo and associated mesoscale vortex that were responsible for producing an extensive swath of high winds across Kansas, southern Missouri, and southern Illinois on 8 May 2009 is presented. The simulation was able to reproduce many of the key attributes of the observed system, including an intense [~100 kt (51.4 m s^{-1}) at 850 hPa], 10-km-deep, 100-km-wide warm-core mesovortex and associated surface mesolow associated with a tropical storm–like reflectivity eye. A detailed analysis suggests that the simulated convection develops north of a weak east–west lower-tropospheric baroclinic zone, at the nose of an intensifying low-level jet. The system organizes into a north–south-oriented bow echo as it moves eastward along the preexisting baroclinic zone in an environment of large convective available potential energy (CAPE) and strong tropospheric vertical wind shear. Once the system moves east of the low-level jet and into an environment of weaker CAPE and weaker vertical wind shear, it begins an occlusion-like phase, producing a pronounced comma-shaped reflectivity echo with an intense warm-core mesovortex at the head of the comma. During this phase, a deep strip of cyclonic vertical vorticity located on the backside of the bow echo consolidates into a single vortex core. A notable weakening of the low-level convectively generated cold pool also occurs during this phase, perhaps drawing parallels to theories of tropical cyclogenesis wherein cold convective downdrafts must be substantially mitigated for subsequent system intensification.

1. Introduction

During the morning of 8 May 2009, a large bow-echo system developed over western Kansas and proceeded eastward, spawning multiple tornadoes and packing surface winds of 70–90 kt (36.0–46.3 m s^{-1}, where 1 kt = 0.514 m s^{-1}) over a swath of up to 150 km wide over an 8-h period before weakening in southern Illinois (e.g., Coniglio et al. 2011, their Fig. 1). Such convectively produced windstorms are often referred to as derechoes (Johns and Hirt 1987) and are quite common across the plains and midwestern United States (e.g., Bentley and Mote 1998; Coniglio and Stensrud 2004). The 8 May event, however, was no ordinary derecho. During its most intense phase, the bow echo appeared to occlude, producing a warm-core eyelike structure similar to those observed with tropical cyclones (e.g., Fig. 1a). Much of the wind damage with this system was associated with an intense ($\Delta p \sim 8$ hPa) mesolow located at the northern tip of the bow well behind the leading gust front. Many of the key structures of this convective system were forecast in real time 24 h in advance, including the occluded eyelike structure and accompanying intense mesolow (Fig. 1b), using the Advanced Research core of the Weather Research and Forecasting Model (WRF-ARW; Skamarock et al. 2008) with a 3-km horizontal grid interval and explicit convection. This simulation allows for an unprecedented opportunity to study such a unique convective system, to help clarify its kinematic and thermodynamic character as well as the environmental factors that may have been keys to its development. In the following, we present an overview of

* Current affiliation: Atmospheric Science Group, University of Wisconsin—Milwaukee, Milwaukee, Wisconsin.

+ The National Center for Atmospheric Research is sponsored by the National Science Foundation.

Corresponding author address: Morris L. Weisman, National Center for Atmospheric Research, P.O. Box 3000, Boulder, CO 80307-3000.
E-mail: weisman@ucar.edu

DOI: 10.1175/WAF-D-12-00023.1

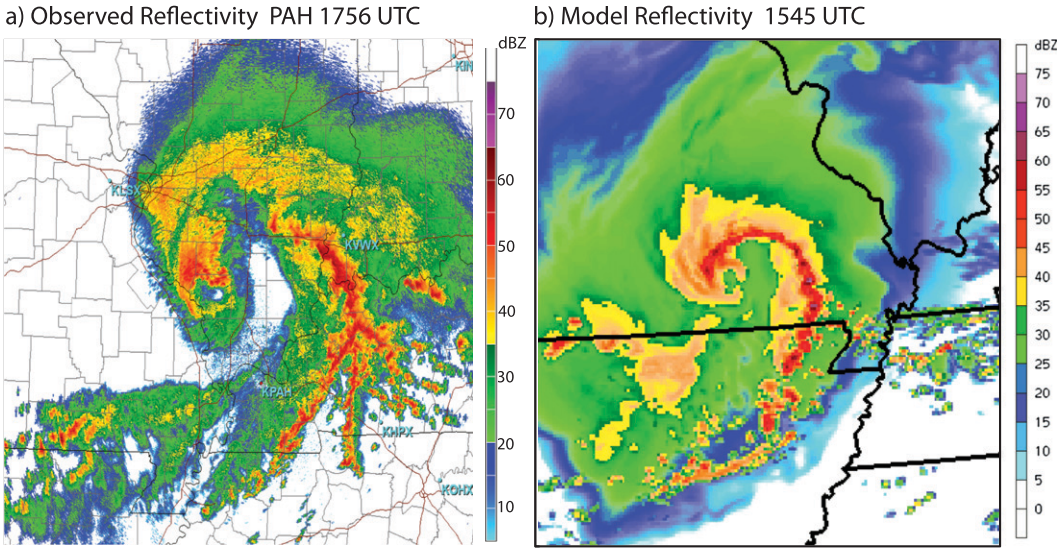

FIG. 1. (a) Paducah, KY (PAH), Weather Surveillance Radar-1988 Doppler (WSR-88D) level II 0.5° radar reflectivity (dB*Z*) at 1756 UTC 8 May 2009. (b) Column maximum derived reflectivity (dB*Z*) from 27-h 3-km WRF-ARW real-time forecast, valid at 1545 UTC 8 May 2009.

this simulated system, highlighting the convective and environmental features that may have contributed to its unique structure and evolution.

The occurrence of mesoscale vortices in association with convective systems is not uncommon. Such features were first highlighted by Fujita (1978), who described the evolution of a bow-shaped convective line from a symmetric to comma-shaped structure over several hours, with the northern comma head associated with notable cyclonic rotation of radar reflectivity features. More generally, such symmetric to asymmetric evolution associated with the development of a dominant northern-end cyclonic vortex is generic to many linear convective systems, severe and nonsevere alike (e.g., Houze et al. 1989; Loehrer and Johnson 1995). Such mesovortices can further evolve into a balanced mesoscale convective vortex (MCV) within the stratiform region of the decaying system, sometimes lasting for several days and being instrumental in triggering subsequent convective outbreaks (e.g., Raymond and Jiang 1990; Menard and Fritsch 1989; Bartels and Maddox 1991; Davis and Trier 2007; Trier and Davis 2007). Such long-lasting MCVs tend to maximize in strength in the midtroposphere, with generally only weak reflections of the circulation extending to the surface after the associated cold pool has weakened (e.g., Bosart and Sanders 1981; Fritsch et al. 1994; Rodgers and Fritsch 2001; Davis and Trier 2002; Davis and Galarneau 2009).

Although severe straight-line winds and tornadoes associated with convective lines and bow echoes tend to occur most often along the leading edge of the system (e.g., Atkins et al. 2004, 2005; Wheatley et al. 2006; Wakimoto et al. 2006a,b), there have also been notable occurrences more directly associated with the northern cyclonic bookend vortex (e.g., Przybylinski and Schmocker 1993; Pfost and Gerard 1997; Atkins et al. 2004). In some of these cases, the intensification of the vortex seemed to be associated with either the transition of a high-precipitation (HP) type supercell embedded within the line into a rotating comma head (e.g., Doswell et al. 1990; Moller et al. 1990; Funk et al. 1999) or with the merger of the line with more isolated, supercell-type storms ahead of the encroaching bow echo (e.g., Sieveking and Przybylinski 2004; Wolf 1998). A notable attribute of all of these cases is the wrapping up of the northern radar reflectivity pattern into a comma-shaped echo, although usually at a scale much smaller than observed for the 8 May 2009 event. There have been some recent notable examples perhaps similar to the 8 May event, however. The 15 July 1995 bow-echo event in northern New York State, which produced one of the largest tree blow downs in history in the Adirondacks (e.g., Cannon et al. 1998; Bosart et al. 1998), was also largely associated with a northern bookend vortex and associated comma-shaped echo closer in scale to the 8 May event. Roth (2003) describes a severe event on 21 July 2003 in Pennsylvania and southern New York State that produced an apparent ''eye'' in association with a northern cyclonic bookend vortex comparable in size to the 8 May event. Although not as intense in terms of surface wind production, the 6–7 May 1985 mesoscale convective system observed during the Preliminary Regional Experiment

for STORM-Central (PRE-STORM) represents a well-documented example of a squall line in which an intense convectively generated mesoscale vortex produces a pronounced comma-shaped echo (e.g., Brandes 1990).

Idealized simulations to date have been successful in reproducing many of the observed characteristics of bowing convective systems, including both bookend (line end) vortices (e.g., Weisman 1993; Weisman and Davis 1998; Cram et al. 2002) and leading-line mesoscale vortices (e.g., Weisman and Trapp 2003; Trapp and Weisman 2003; Atkins and Laurent 2009). These simulations have also shown that the preferential development of a cyclonic bookend vortex over several hours can simply result from the midtropospheric convergence of planetary vorticity (e.g., Skamarock et al. 1994). Such simulated bookend vortices, however, tend to display very little reflection down to the surface. This may be related to the simple unidirectional shear profiles that have generally been employed in these idealized studies or to the very cold surface cold pools that were produced in these simulations. Leading-line cyclonic mesoscale surface vortices are readily produced in such simulations, but, again, only in the presence of the convergence of planetary vorticity. Such leading-line vortices are sometimes observed to merge with the northern cyclonic bookend vortex but do not maintain a reflection to the surface if they propagate behind the system into the cold outflow air. Atkins et al. (2004) and Wheatley and Trapp (2008) similarly show the development of a range of leading-line mesoscale vortices within simulations of observed convective systems but, again, these cases were not characterized by the development of an intense mesoscale bookend vortex and attendant occluded surface mesolow, as was observed on 8 May.

The goal of the present paper is to use the successful WRF simulation as a surrogate for the observed event to better establish its basic structural character and relationship to the environment, and to serve as the foundation and motivation for more detailed analyses to come. We begin with a brief overview of the observed and simulated event, emphasizing the key synoptic and mesoscale features that may have contributed to its unique structure and evolution. We then proceed to a more detailed analysis of the simulated event, tracing the evolution of key thermodynamic and kinematic features from its onset in western Kansas as a more typical asymmetric leading-line trailing-stratiform convective system to its occlusion-like stage in Missouri with an intense warm-core mesovortex. In the process, we note that the basic kinematic structure of the system, composed of an intense rear-inflow jet and a deep strip of cyclonic vorticity extending from the northern bookend vortex southward along and within the cold pool, becomes established very early in the evolution of the system. The transition to the occlusion-like stage is, somewhat surprisingly, associated with a weakening of the convective line and associated convective cold pool as the system moves east of the low-level jet (LLJ) into an environment of weaker vertical wind shear and CAPE. These results will then be discussed within the context of past observational and modeling studies of severe bow-echo systems.

2. Real-time WRF-ARW forecasts

Since 2003, real-time explicit convective forecasts at 3–4-km grid spacing have been run at NCAR during each spring to establish the capabilities of the WRF-ARW modeling system (e.g., Skamarock and Klemp 2008) to forecast severe convective events and to test recent model improvements (e.g., Done et al. 2004; Weisman et al. 2008). These forecasts have also been evaluated yearly alongside a host of forecasts obtained from differing modeling configurations and dynamical cores by a variety of modeling groups as part of the Storm Prediction Center (SPC) and National Severe Storms Laboratory (NSSL) Hazardous Weather Test Bed (HWT) Spring Experiment (e.g., Weiss et al. 2004; Kain et al. 2005, 2006, 2008; Coniglio et al. 2010; Clark et al. 2011). For the 2009 season, 3-km WRF-ARW forecasts were produced twice a day, initialized at 0000 and 1200 UTC, extending to 48 h. Initial conditions were supplied from the National Oceanic and Atmospheric Administration/Earth System Research Laboratory (NOAA/ESRL) high-resolution (13 km) operational Rapid Refresh (RR) model with boundary conditions supplied by operational Global Forecast System (GFS) forecasts. Retrospective sensitivity studies also considered initializations using both the North American Mesoscale (NAM) and GFS model analyses.

Physics parameterizations included the Mellor–Yamada–Janjić (MYJ) boundary layer scheme (Janjic 2001), the unified Noah land surface model (Chen and Dudhia 2001), and the Thompson microphysics scheme (Thompson et al. 2006). Radiation effects were parameterized using the rapid radiative transfer model (RRTM) for longwave radiation (Mlawer et al. 1997) and the Dudhia (1989) scheme for shortwave radiation. Positive-definite transport was specified for the moisture variables, thereby reducing the positive precipitation biases that have been noted in such high-resolution convective forecasts (e.g., Skamarock and Weisman 2009). Retrospective sensitivity testing also considered comparisons between the MYJ versus Yonsei University (YSU; Hong et al. 2006) boundary layer schemes, and Thompson versus the WRF single-moment six-class (WSM6; Hong and Lim 2006) microphysics schemes.

Each of the 18 WRF-ARW retrospective sensitivity experiments that we conducted starting 24 h or less ahead of the observed event indicated that a strong convective system would likely develop over western Kansas overnight, and proceed eastward though Missouri, Illinois, and Kentucky the next morning. However, only a couple of these forecasts suggested the unique character and intensity of the observed event. The best of these forecasts was the real-time forecast initialized at 1200 UTC on 7 May using the standard real-time configuration for the 2009 season. The emphasis of the present paper is on the analysis of this successful forecast. Forecast sensitivities for this event will be presented in a forthcoming study.

3. Overview of the observed and simulated event

A detailed study of the early evolution of the 8 May 2009 derecho can be found in Coniglio et al. (2011). The large-scale environment consisted of a strong upper-level jet stream situated north of the eventual convective region with evidence of a weak upper-level wave propagating across Wyoming and northeast Colorado. This wave helped to trigger weak convection from northeast Colorado into western Nebraska and northwest Kansas during the late afternoon and evening hours of 7 May but does not appear to have been a significant contributor to the eventual derecho event. Most unstable convective available potential energy (MUCAPE) magnitudes were quite low in central Kansas, but increased to in excess of 3000 J kg^{-1} in southern Kansas [from Rapid Update Cycle (RUC) analyses; not shown]. The low-to-midlevel vertical wind shear was also quite strong in central and western Kansas (30–50 kt over the lowest 6 km AGL) and generally oriented west to east. Such environmental conditions are commonly observed with severe nocturnal convection and/or derecho events (e.g., Johns and Hirt 1987; Evans 1998; Bentley and Mote 1998; Evans and Doswell 2001; Coniglio and Stensrud 2001; Trier et al. 2006). However, Coniglio et al. (2011) note that while the vertical wind shear was quite strong for the northern portion of the system in central Kansas, it was more nearly average for the portion of the system extending farther to the south. Furthermore, they note an unusually strong, deep, and spatially extensive LLJ with high precipitable water, and very large midlevel lapse rates.

The primary convection associated with the derecho initiated between 0700 and 0800 UTC in central Kansas (Fig. 2a) as the region of weaker convection in northwest Kansas moved southeastward toward the northern terminus of the low-level jet and the associated higher MUCAPE environment. The convection initially organized as an east–west line segment but reoriented into a north–south line segment over several hours (e.g., Figs. 2b,c), extending southward into the higher CAPE environment. Localized severe surface winds commenced during this period associated with a convectively generated cold pool. By 1200 UTC (Fig. 2c), the system had taken on the characteristics of a large, asymmetric bow echo with mesoscale cyclonic rotation evident at the northern end of the bow (evident from radar animations; not shown) and an extensive region of stratiform precipitation extending rearward. A less organized line of convection was also evident extending eastward from the northern mesoscale cyclonic circulation center. Such regions of more disorganized convection extending ahead of a developing bow echo are commonly observed with such bow-echo systems (e.g., Johns and Hirt 1987; Przybylinski 1995) and are often indicative of a larger-scale region of warm advection, as is commonly observed with mesoscale convective systems (e.g., Maddox 1980). A mesoscale surface analysis at 1300 UTC (Fig. 3a) depicts many of the classic signatures of such systems, including a presquall mesolow, a mesohigh associated with a modest surface cold pool ($\Delta\theta \sim 6$ K) (e.g., Engerer et al. 2008), and a wake low to the northwest behind the mesohigh (e.g., Johnson and Hamilton 1988; Loehrer and Johnson 1995).

After 1200 UTC, the bow-shaped convective line grew significantly into a classic comma-shaped echo as it moves rapidly eastward across southern Missouri (Figs. 2d,e). The cyclonic circulation at the northern tip of the system also became more evident during this period, with widespread damaging surface winds now largely located on the western side of this mesoscale vortex, well behind the leading-line gust front, in addition to more isolated regions of strong surface winds and tornadoes still being observed along the gust front. A surface mesoanalysis at 1500 UTC (Fig. 3b) suggests that the mesoscale vortex exhibited an 8–10-hPa pressure minimum at this time, with maximum surface winds estimated between 80 and 90 kt (e.g., from Storm Prediction Center storm reports). These strong surface winds were occurring despite an apparent weakening of the surface cold pool to $\Delta\theta \sim 2$–4 K during this period, emphasizing the potential significant role of the mesovortex in contributing to the intense surface winds for this case. This mesovortex and associated surface mesolow continued to maintain its strength over the next several hours as it progressed northeastward into southern Illinois and western Kentucky (Fig. 2f), occasionally exhibiting an eyelike structure and continuing to produce damaging surface winds of 80–90 kt.

An overview of the reflectivity evolution for the WRF-ARW forecast of this event is presented in Fig. 4.

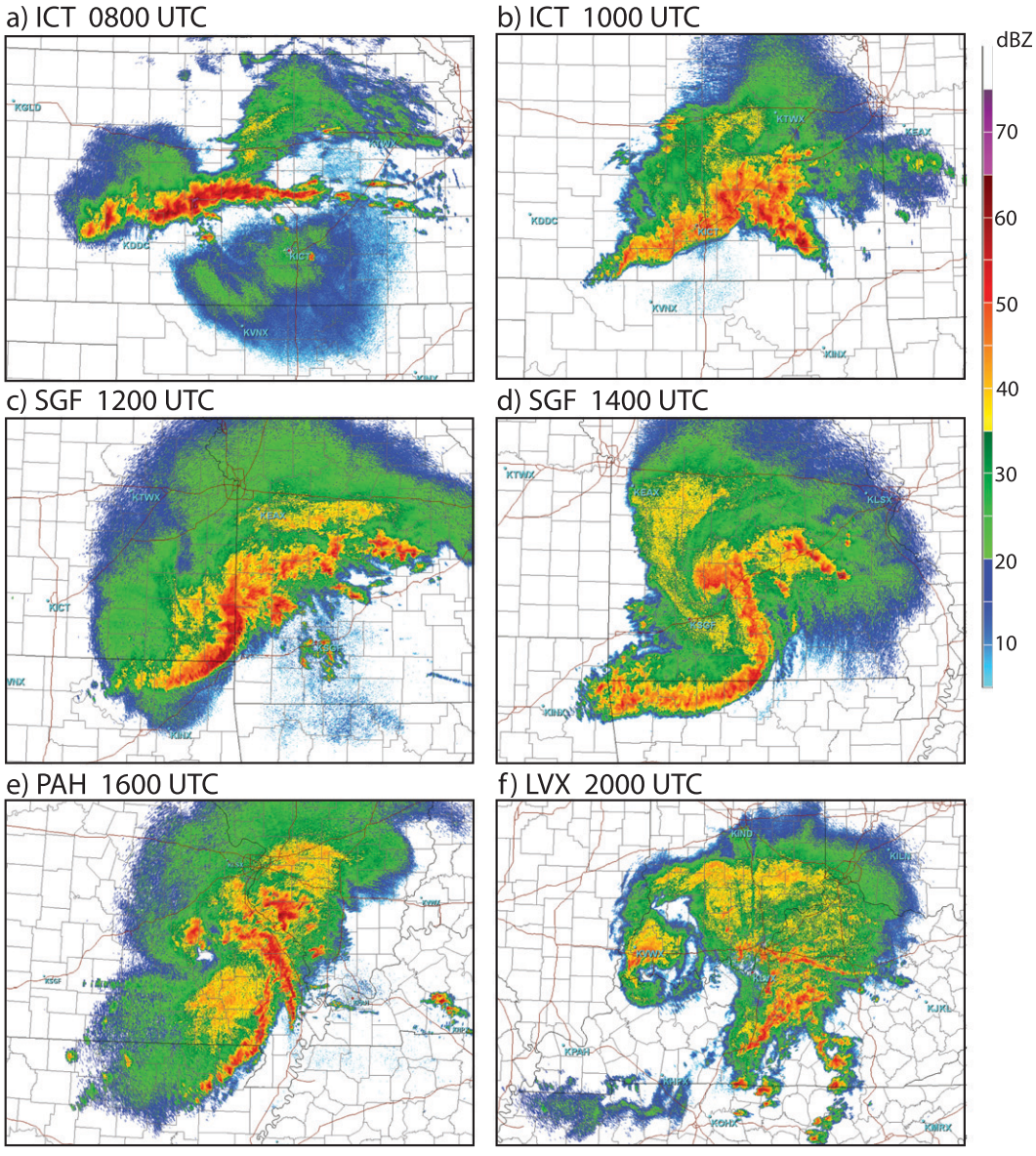

FIG. 2. WSR-88D level II 0.5° radar reflectivity (dB*Z*; shaded) observed at (a) 0800 and (b) 1000 UTC at Wichita, KS (ICT); (c) 1200 and (d) 1400 UTC at Springfield, MO (SGF); (e) 1600 UTC at PAH; and (f) 2000 UTC at Louisville, KY (LVX), on 8 May 2009.

In comparison with the observed system (Fig. 2), the simulated system develops about 2 h earlier and a bit farther southwest than the observed system (e.g., Figs. 2a, 4a). Additionally, while the simulated system has developed a north–south-oriented bow-shaped line by 0600 UTC, the observed system maintains a more east–west orientation through its early evolution (e.g., Figs. 2a,b), not developing a north–south orientation till nearly 1200 UTC (Fig. 2c). Other notable differences include the development of NW–SE-oriented bands ahead of the observed system versus a single, east–west-oriented band extending east of the simulated system. Also, as noted above, the observed system developed a series of leading-line mesovortices (not shown), many of which were associated with enhanced surface wind gusts and tornadoes. Such smaller-scale mesovortices were largely absent from the simulated system, possibly due to the relatively coarse 3-km grid spacing employed. However, it will be shown that the simulated leading-line convection was associated with a strong strip of cyclonic vorticity, which could contribute in a dynamically similar manner as the smaller observed mesovortices. All in all, the similarity in

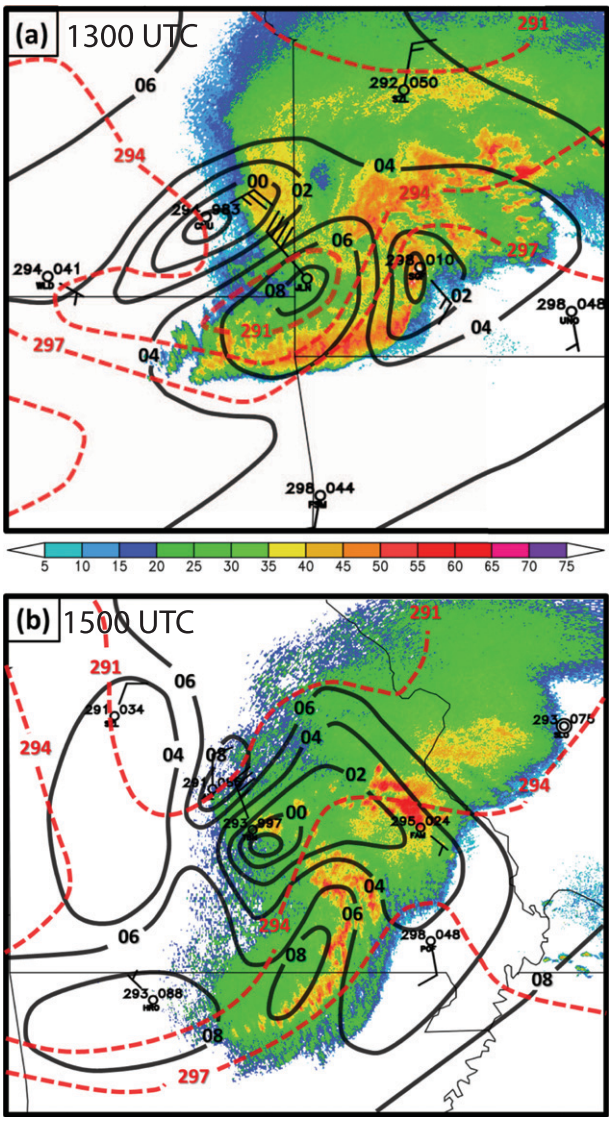

FIG. 3. Surface mesoanalysis at (a) 1300 UTC, with WSR-88D level II 0.5° radar reflectivity (dBZ, shaded) from SGF, and (b) 1500 UTC, with WSR-88D level II 0.5° radar reflectivity from PAH, on 8 May 2009. Solid contours represent surface pressure isobars at 2-mb intervals, with dashed contours representing potential temperature isotherms at 3-K intervals. Only select surface observations are included for clarity. Also, no attempt was made to incorporate convective-scale observations into the analysis, which would likely tighten and relocate the analyzed pressure and potential temperature gradients somewhat relative to the radar-depicted features.

the evolution of the reflectivity field, including the eventual development of the comma head and associated intense mesovortex, suggests that the basic character of the observed event is reasonably captured by the simulation.

A more detailed description of the model forecast begins at 0600 UTC, after the simulated convection in west-central Kansas has evolved into two small north–south-oriented bow-shaped segments (Fig. 4a). The larger-scale model environment at this time exhibits a 50–75-kt westerly jet at 500 mb in northeast Colorado and Nebraska, weakening to 30–40 kt to the south in Texas and Oklahoma (Fig. 5a). A weak north–south potential temperature gradient accompanies this jet structure, with the strongest gradient evident in Nebraska in association with the jet core. A weak trough is evident at 700 hPa in southwest Kansas and the Oklahoma panhandle (Fig. 5b), with an enhanced north–south potential temperature gradient extending eastward into central Kansas. This trough is more evident at 850 hPa (Fig. 5c) and is associated with a thermal ridge extending southward through the Texas Panhandle and a 50-kt southerly low-level jet situated just east of the thermal ridge. With the low-level jet and midtropospheric baroclinicity in place, warm-air advection is evident throughout southern and central Kansas (e.g., Maddox 1980). A sharp north–south gradient in MUCAPE (defined here as the maximum CAPE in the lowest 3000 m AGL) is also evident extending eastward through southern Kansas (Fig. 5d), ranging from over 3000 J kg^{-1} to the south, reducing to 250–750 J kg^{-1} farther to the north. This MUCAPE gradient is associated with weak diffluence–convergence in the low-to-midlevel wind field (Figs. 5b,c). The 0–6-km AGL vertical wind shear vectors at this time point generally west to east, with magnitudes ranging from 40 to 50 kt over southwestern Kansas, just south of the developing convection, decreasing to 30–40 kt farther to the east in Kansas and to the south over Oklahoma (Fig. 5d).

By 1000 UTC (Fig. 4b), the modeled convective system has consolidated into a single, north–south-oriented bow echo in southeast Kansas and northern Oklahoma. Convection also extends eastward from the northern end of the bow, along the preexisting midtropospheric baroclinic zone and associated north–south gradient in MUCAPE, as was also observed (e.g., Fig. 2b). Model analyses at 1200 UTC (Fig. 6) suggest that the convective system has now moved east of the 850- and 700-hPa trough features that were evident earlier, and is also beginning to move east of the low-level jet, which had veered during the night. Perhaps more noteworthy, the system is beginning to propagate into an environment of weaker tropospheric vertical wind shear, MUCAPE, and midtropospheric baroclinicity. By 1400 UTC (Fig. 4c), the system is now located in southern Missouri and has developed into a large comma-shaped feature. This system maintains its structure and strength as it propagates eastward into southern Illinois before eventually weakening over Kentucky (Fig. 4d).

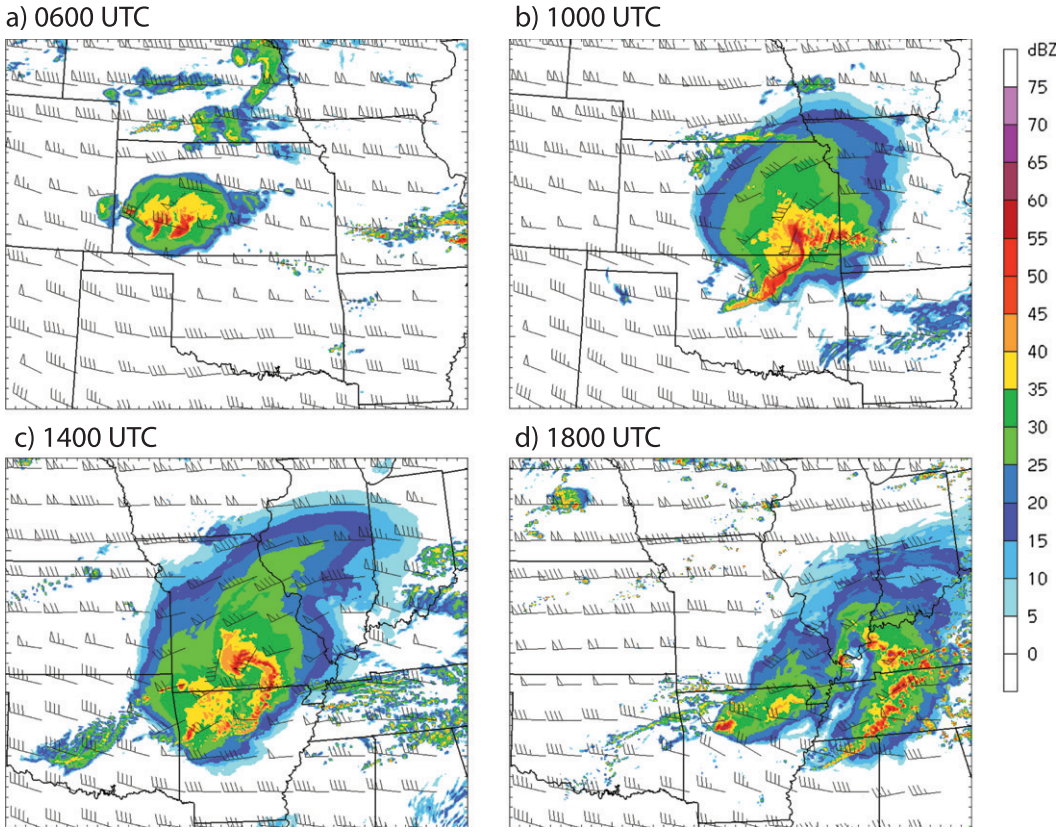

FIG. 4. Column maximum derived radar reflectivity (dBZ; shaded) and 300-hPa winds (kt) from the 3-km WRF-ARW real-time forecast initialized at 1200 UTC 7 May 2009, valid at (a) 0600, (b) 1000, (c) 1400, and (d) 1800 UTC, representing 18-, 22-, 26-, and 30-h forecasts, respectively. Wind barbs are spaced every 35 grid points (105 km). Only a 1350 km × 1080 km portion of the full domain is shown.

4. Mesoscale and convective-scale structure and evolution

Figures 7–11 present finer-scale model analyses at 2-h intervals from 0900 to 1500 UTC. By 0900 UTC, north-to-northwesterly surface winds in excess of 60 kt are evident behind the northern portion of the convective system (Fig. 7b). At this time, the surface pressure field (Fig. 8a) exhibits a classic pattern associated with asymmetric convective systems, including a 993-hPa presquall mesolow, 1010-hPa mesohigh, and 994-hPa wake low (e.g., Johnson and Hamilton 1988). This surface pressure pattern is also quite similar to the observed surface pressure field at 1300 UTC (Fig. 3a), although the simulated features appear to be a bit too strong. Other key simulated features at 0900 UTC include a cold pool extending upward through 700 hPa and an intense west-to-northwesterly elevated rear-inflow jet reaching magnitudes of over 80 kt (e.g., Figs. 9a, 10a, 11a). A region of notable warming is evident at 850 hPa collocated with the surface wake low on the northwest side of the system (Figs. 8a, 10a), indicative of descending motion at that location.

Strong convergence and cyclonic shear are evident along the leading edge of the cold pool (e.g., Figs. 8a, 9a, 10a) and are especially strong at the northern end of the system where the cold pool intersects the preexisting zonally oriented lower-tropospheric boundary. An east–west vertical cross section through the northernmost cell at this time (Figs. 12a–c) depicts a leading-line–trailing stratiform reflectivity structure (Fig. 12a) with weaker convective cells evident to the east along the preexisting baroclinic zone noted above. The cold pool extends up to nearly 4 km AGL (Fig. 12b), with cyclonic shear evident along the gradient between the high- and low-θ_e air. An east–west vertical cross section taken farther south through the apex of the bow (Figs. 12d–f) depicts a shallower and somewhat weaker cold pool and cyclonic shear zone. Storm-relative wind and θ_e analyses at 0900 UTC (Fig. 13) depict a strong north–south gradient in θ_e extending through 850 hPa ahead of the system with low-θ_e air extending upward to 850 hPa within the

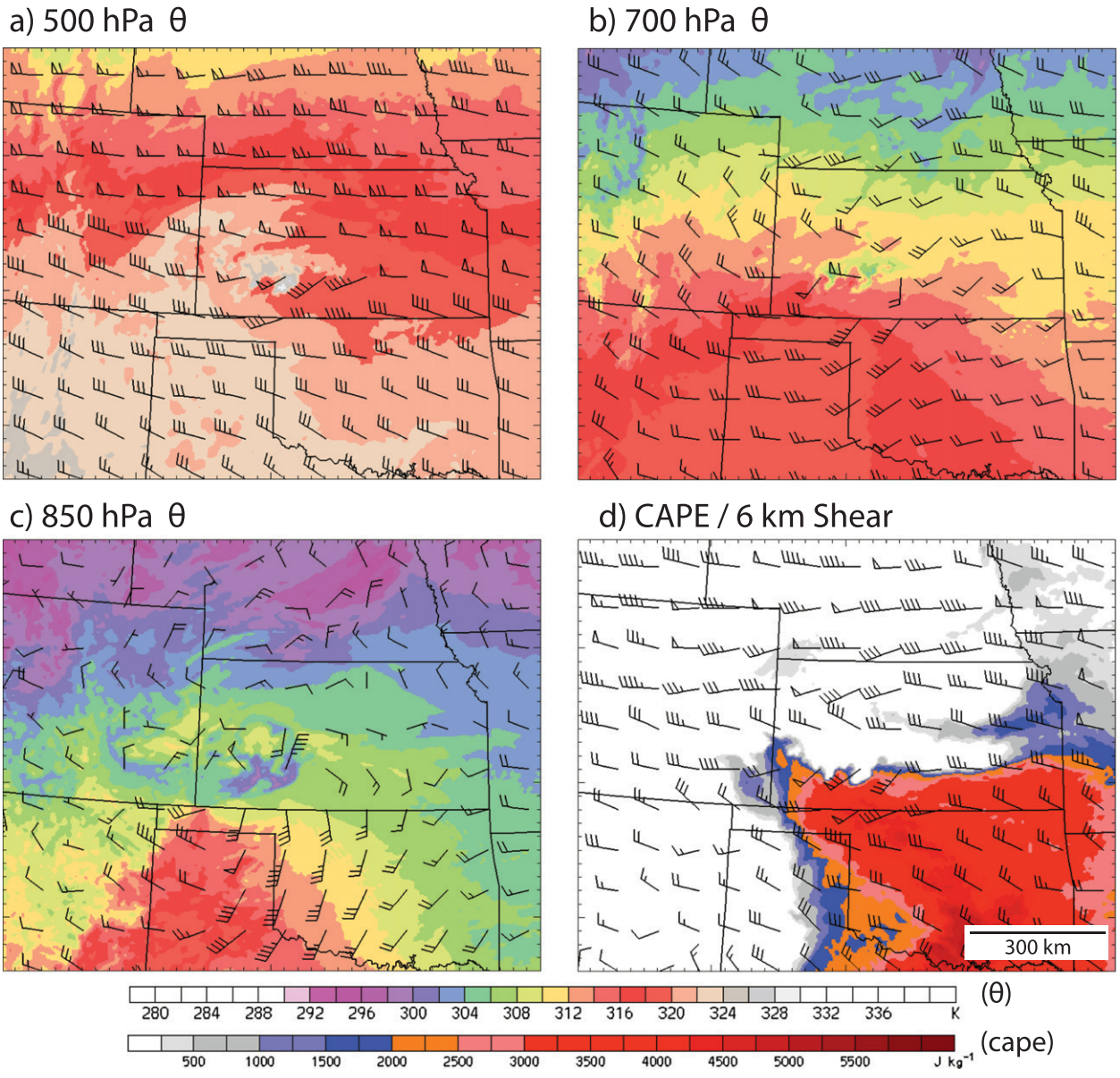

FIG. 5. Winds and potential temperatures at (a) 500, (b) 700, and (c) 850 hPa, along with (d) maximum boundary layer CAPE and 0–6-km AGL vertical wind shear, from the 3-km WRF-ARW real-time forecast initialized at 1200 UTC 7 May 2009, valid at 0600 UTC 8 May 2009 (18-h forecast). Wind barbs (kt) are spaced every 30 grid points (90 km). Potential temperature is shaded at 2-K intervals. Vertical wind shear is presented as the bulk vector difference in wind magnitude (kt) between the surface and 6 km AGL. Only a 1200 km × 960 km portion of the full domain is shown.

system cold pool. High-θ_e air is also evident at both 700 and 500 hPa along and rearward of the leading edge of the system (e.g., Figs. 13c,d), indicative of the upward transport by convective updrafts.

The key flow components of the system at this time are better established via the use of system-relative trajectories (Fig. 14). These trajectories are calculated with the RIP software for model output (Read/Interpolate/Plot users' guide available online at http://www.mmm.ucar.edu/wrf/users/docs/ripug.htm), using a 5-min integration interval and applying linear interpolation in both time and space. Each trajectory extends over a 3-h time period from each point and time of origin. The accuracies of the trajectories were checked by assuring consistent results within several grid intervals of each point of origin as well as by checking for a reasonable conservation of θ_e along the trajectories, at least away from regions of strong temperature and moisture

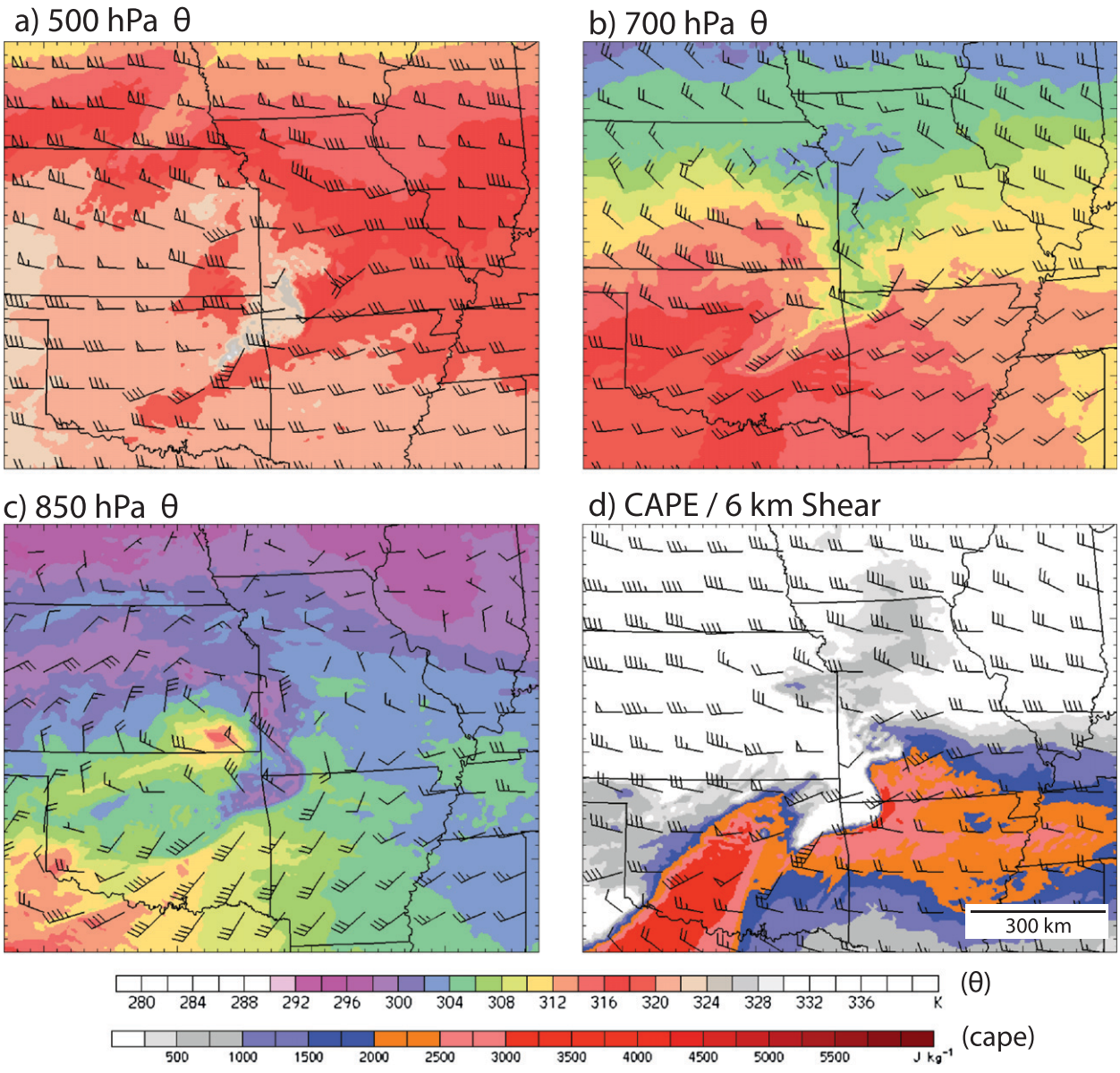

FIG. 6. As in Fig. 5, but valid at 1200 UTC 8 May 2009 (24-h forecast).

gradients. Three sets of trajectories are presented as being representative of a much larger set that were considered: forward trajectories originating at 0.5 km in the warm, high-θ_e air mass ahead of the system; backward trajectories originating at 0.75 km within the cold pool; and backward trajectories originating at 3 km surrounding the northern cyclonic bookend cell, which eventually evolves into the intense mesoscale vortex.

As could also be inferred from Fig. 13, high-θ_e inflow trajectories mostly originate at low levels from the southeast (within the system-relative framework) and rise abruptly upon encountering the leading edge of the gust front (Fig. 14b). Most of the air parcels that populate the cold pool at low levels at this time originate from midlevels, to the north of the east–west baroclinic zone, and descend while turning southward cyclonically around the northern bookend cell (Fig. 14c). Parcels that populate the midlevels surrounding the northern bookend cell are observed to converge from all directions (Fig. 14d), with parcels on the east side generally ascending from low levels from the east and southeast while those on the west side descend from 6 to 8 km from the northwest.

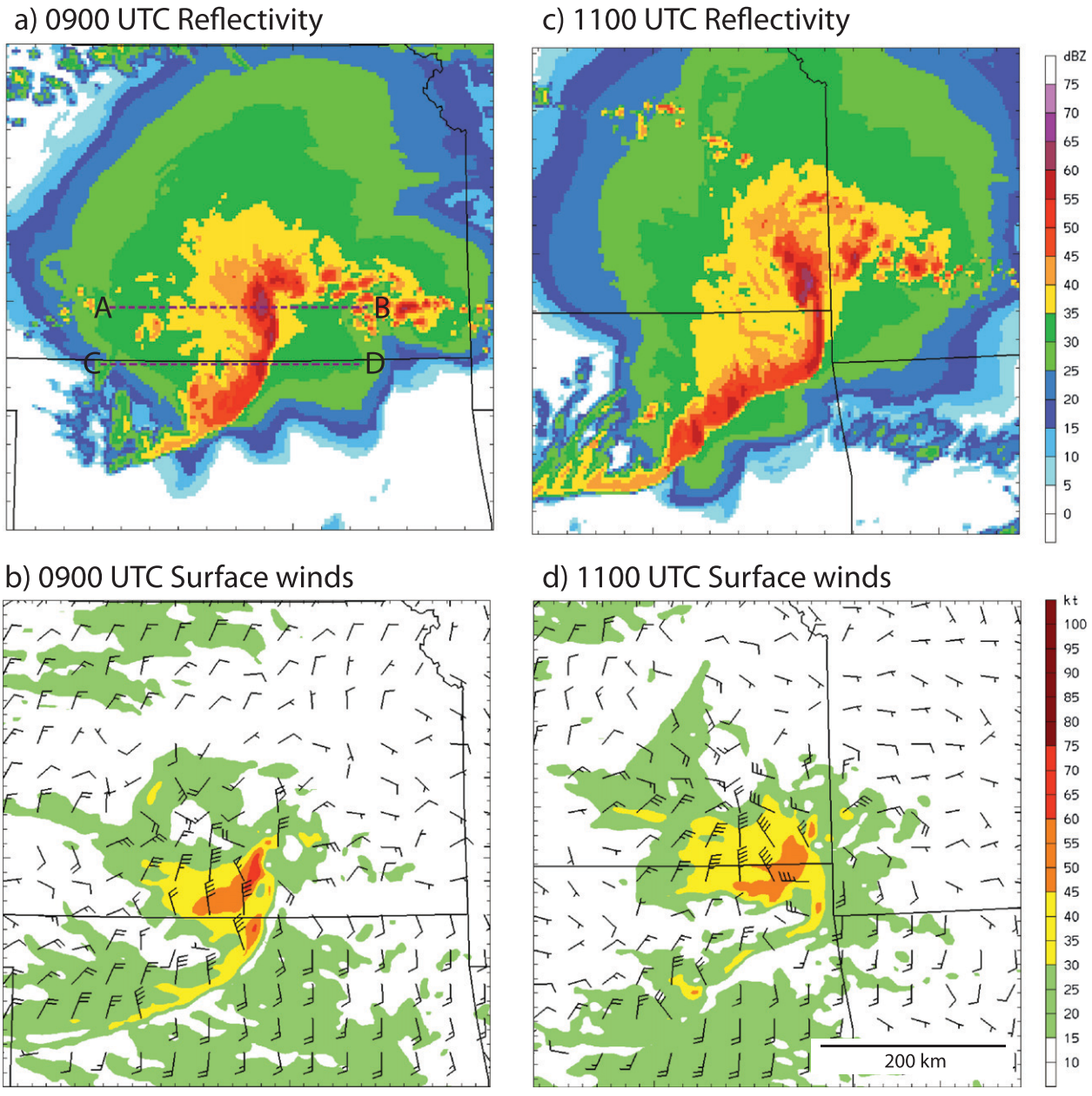

FIG. 7. (a) Column maximum derived reflectivity (dBZ, shaded) and (b) surface winds (kt) at 0900 UTC. [(c),(d)],[(e),(f)],[(g),(h)] As in (a),(b) but for 1100, 1300, and 0015 UTC on 8 May 2009, from the 3-km WRF-ARW real-time forecast initialized at 1200 UTC 7 May 2009. Surface wind barbs (kt) are spaced every 12 grid points (36 km), with the surface wind magnitude shaded using a 15-kt interval. Only a 510 km × 510 km portion of the full domain is shown.

The convective system continues to grow larger while maintaining the same basic structural characteristics through 1100 UTC (Figs. 7c,d). Subtle changes include an increase in the warming associated with the wake low on the northwest side of the system (Figs. 9b, 10b) and about 2 K of warming within the cold pool relative to earlier (Figs. 9a,b). Also noteworthy at 1100 UTC is a decrease in potential temperature within the low-level storm-relative inflow as compared to earlier, consistent with the decreasing environmental CAPE (e.g., Fig. 6).

After 1100 UTC, the apex of the bow appears to surge eastward, with the northernmost cell intensifying and the reflectivity field wrapping into a large-scale hook. By 1300 UTC (Figs. 7e,f), this reflectivity hook appears similar to a tropical cyclone eye except for an opening on its south side. By this time, surface winds have weakened

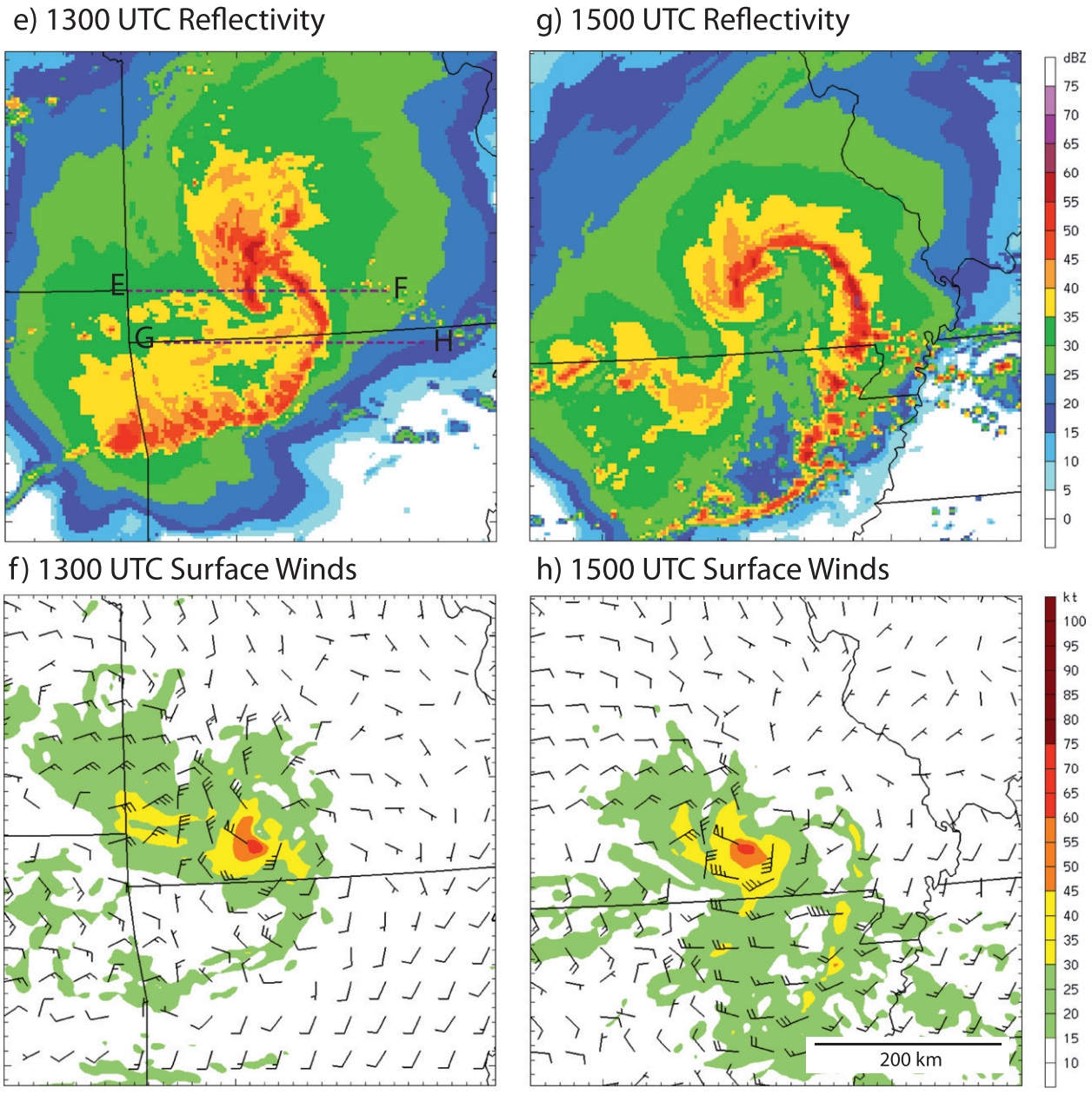

FIG. 7. (*Continued*)

behind the leading edge of the gust front extending to the south. However, a region of over 60-kt surface flow associated with a 989-hPa mesolow (Figs. 7f, 8c) is now located on the southwest side of this eyelike feature, well behind the original convective gust front. A wake low is also still evident farther to the west on the edge of the precipitation region. Again, these simulated surface features are quite consistent with the mesoanalysis at 1500 UTC (e.g., Fig. 3b), although the simulated mesolow and wake low are still somewhat stronger than analyzed. Above the surface, the winds have now intensified to 90–100 kt on the southwest side of the vortex from 925 through 700 hPa (Figs. 9c, 10c, 11c), with relatively warm potential temperatures now evident at the center of the vortex at 700 hPa.

An east–west cross section through the reflectivity hook at 1300 UTC (Figs. 15a–c) now clearly shows a deep warm-core configuration with isentropes sloping downward into the mesovortex center up to 8 km AGL. Low-θ_e values are still evident to the west of the reflectivity

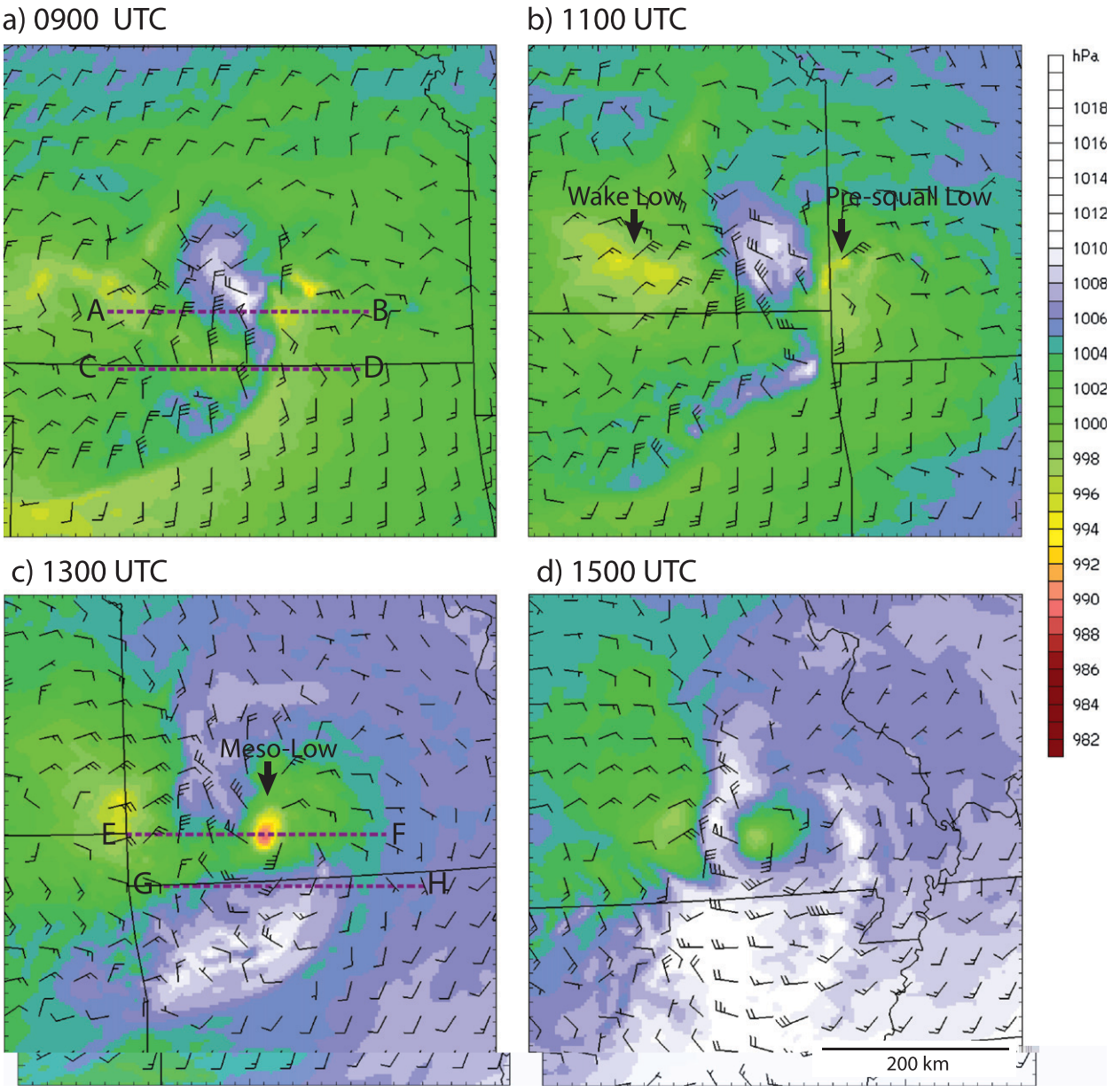

FIG. 8. Simulated surface pressure (hPa, shaded) and surface wind barbs (kt) at (a) 0900, (b) 1100, (c) 1300, and (d) 1500 UTC 8 May 2009 from the 3-km WRF-ARW real-time forecast initialized at 1200 UTC 7 May 2009. Wind barbs are spaced every 12 grid points (36 km). Only a 510 km × 510 km portion of the full domain is shown.

hook (Figs. 15b), with higher θ_e values in the inflow to the east of the system. However, the overall east–west gradient of θ_e is much weaker (15–20 vs 35–45 K) than earlier. Additionally, θ_e appears to be well mixed through the depth of the system near its center. The vertical motion field (Fig. 15c) is characterized by upward motion on the eastern flank of both reflectivity features with downward motion evident in between. Downward motion and downward-sloping isentropes are also evident toward the west edge of the system in association with the wake low.

An east–west vertical cross section through the apex of the bow (Figs. 15d–f) continues to show a strong, elevated rear-inflow jet reaching magnitudes of 105 kt near 3 km AGL. However, the θ and θ_e gradients have weakened considerably from earlier, implying a much weaker surface cold pool. Indeed, the updraft at the leading edge of this portion of the cold pool now appears to be elevated in contrast to the surface-based structure evident earlier. The weakening of the surface cold pool during this phase of evolution represents an

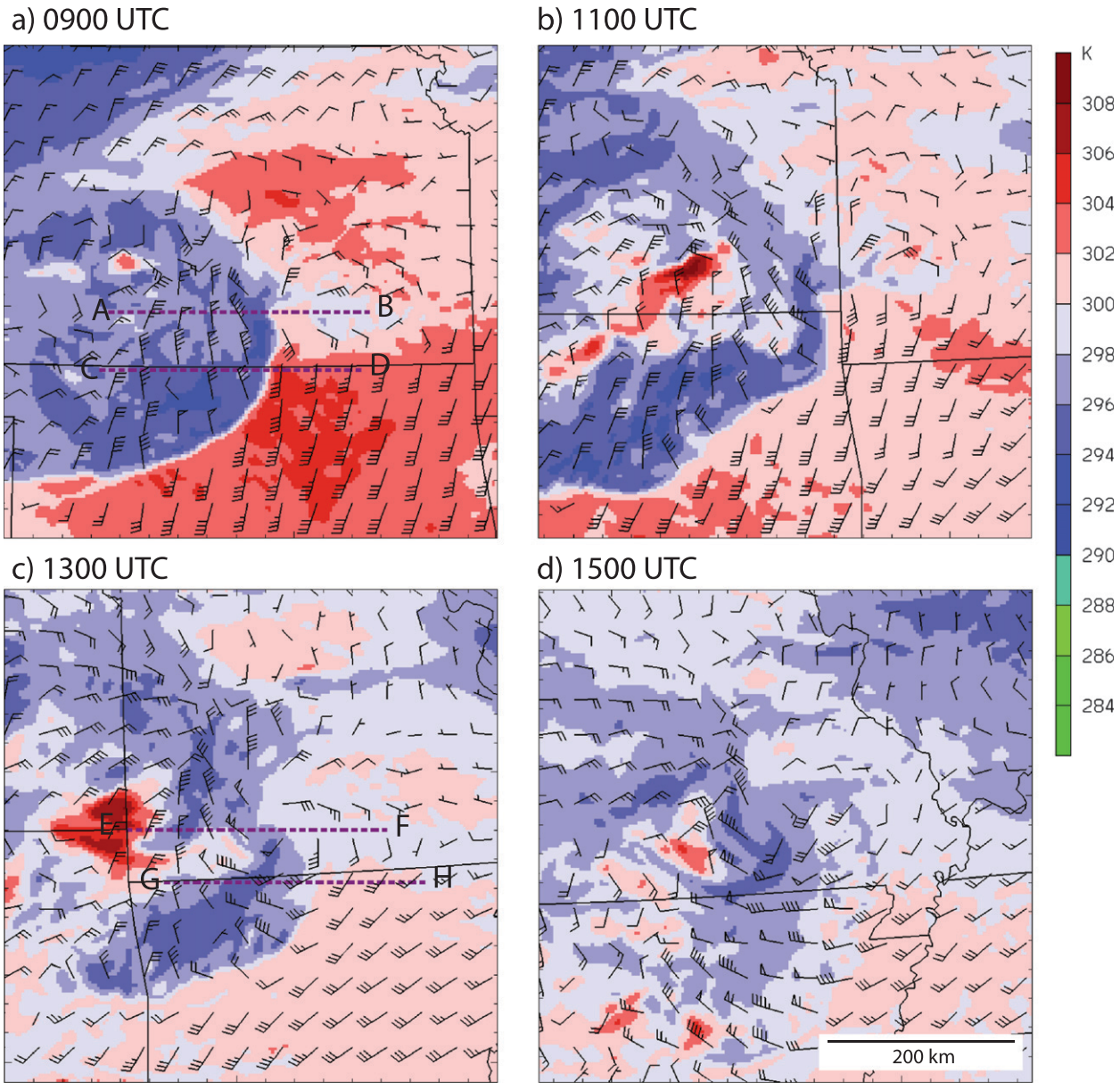

FIG. 9. Simulated potential temperature (shaded) and wind barbs (kt) at 925 hPa at (a) 0900 UTC, (b) 1100 UTC, (c) 1300 UTC and (d) 1500 UTC, as in Fig. 8.

intriguing characteristic of this system and is discussed in more detail below.

The θ_e and system-relative flow at 1300 UTC (Fig. 16) clearly show higher-θ_e air feeding from the east and southeast from the surface through 850 hPa with high-θ_e air also now present within the mesovortex around the northern end of the system. A core of higher-θ_e air is also evident at both 700 and 500 hPa in the core of the mesovortex. Some convergence is still evident along the low-level boundary to the east, but the magnitude of both the convergence and the north–south θ_e gradient appears weaker than at 0900 UTC (e.g., Fig. 13). Low-θ_e air still extends southward through the cold pool, but, again, the θ_e deficits are not as large as at 0900 UTC (e.g., Fig. 13).

Trajectories at 1300 UTC (Fig. 17) also display some notable changes from earlier. In particular, while most inflow parcel trajectories still rise steeply upon encountering the surface cold pool, many of these parcels are now observed to travel northward along the leading edge of the system and become directly incorporated into the northern cyclonic mesovortex (Fig. 17b). Additionally, some of the inflow parcels originating close to the surface (not shown) also now travel through the leading line, ending up at low altitudes within the cold

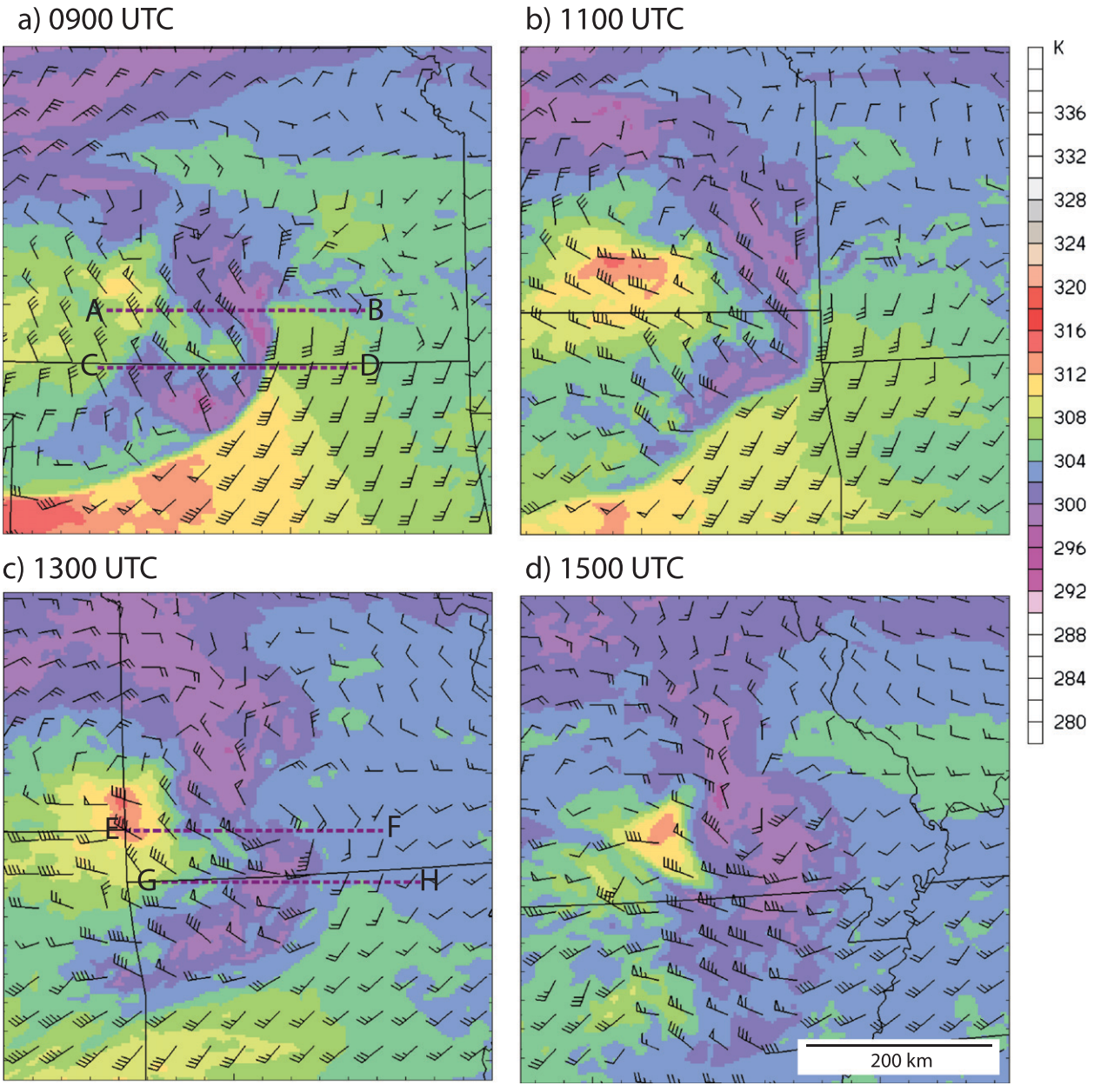

FIG. 10. As in Fig. 9, but at 850 hPa.

pool, suggesting a more elevated character to the inflow at this time, as noted above. Most of the parcels populating the low-level cold pool, however, still originate from north of the preexisting east–west boundary, descending from midlevels while turning cyclonically around the mesovortex (Fig. 17c). A significant number of cold-pool air parcels, though, also now originate from mid- to upper levels from the west, descending within the rear-inflow jet. For the air parcels surrounding the mesovortex at 3 km (Fig. 17d), three primary trajectory streams are now identifiable. One stream ascends from the southeast, bringing higher-θ_e air around the northern and eastern periphery of the mesovortex. A second stream originates from low to midlevels from the east and northeast, from along the eastward-extending baroclinic zone. A third stream descends from the mid- to upper troposphere from the west-northwest, bringing lower-θ_e air to the southern periphery of the mesovortex. Finally, backward trajectories originating from the center of the vortex at 700 and 500 hPa (not shown) clearly show a history of descent (up to 1–2 km) and adiabatic warming over the previous hour,

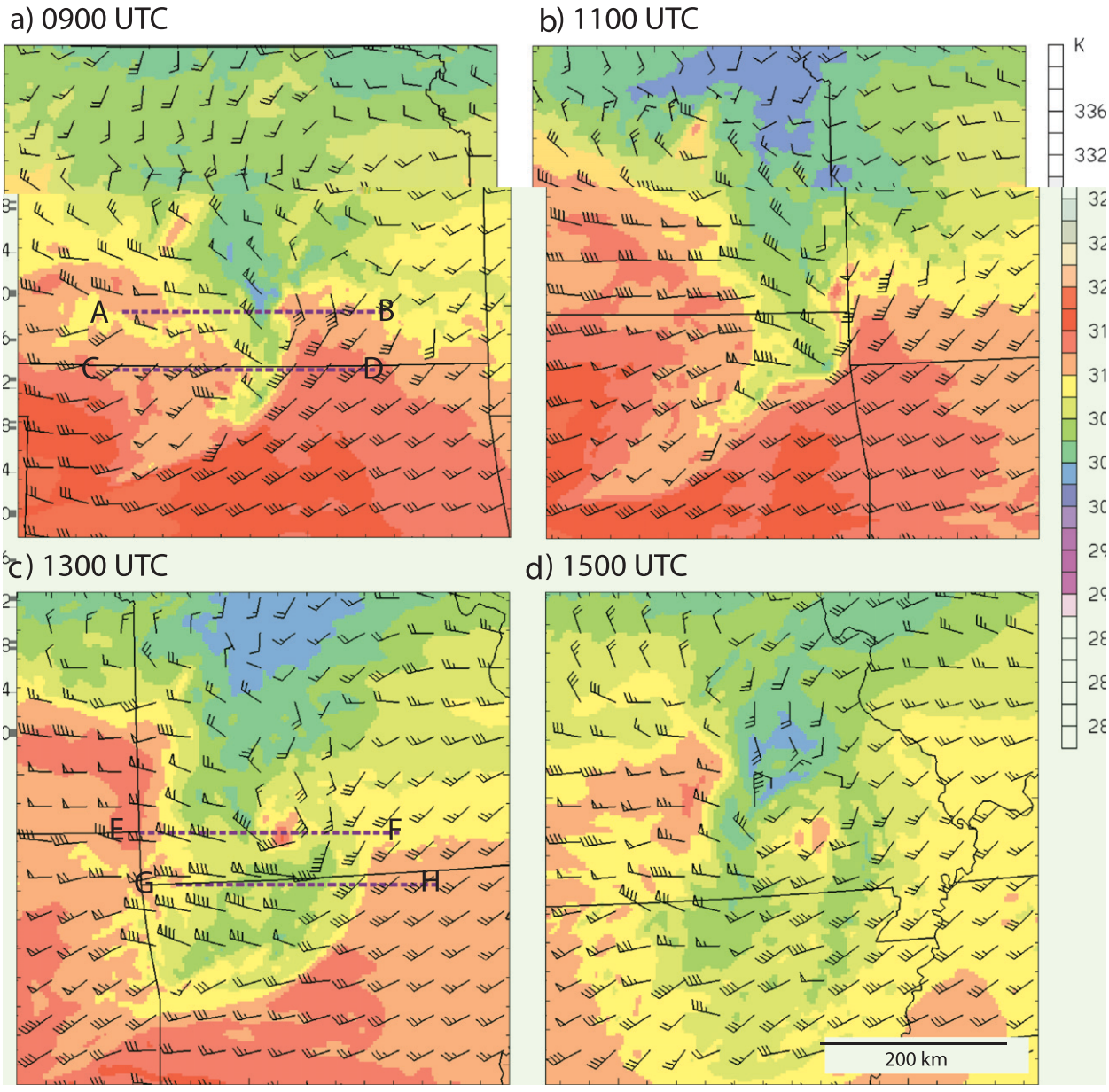

FIG. 11. As in Fig. 9, but at 700 hPa.

likely contributing to the warm-core structure noted above.

The simulated system continues to expand in scale through 1500 UTC (Figs. 7g,h), maintaining a comma-shaped radar configuration in association with a strong, deep mesovortex, and also maintaining a region of intense surface winds in excess of 60 kt on the southwest side of the mesovortex. Both the associated surface mesolow and the wake low at the back edge of the system are still quite evident (Fig. 8d), although the minimum sea level pressures have increased somewhat in both features (e.g., from 988–994 hPa to 996–996 hPa, respectively). A maximum of 85-kt flow is still evident at 925 and 850 hPa above the region of intense surface flow (e.g., Figs. 9d, 10d). The mesovortex still appears as a warm core at 700 hPa (Fig. 11d). Horizontal θ gradients also continue to decrease across the leading edge of the cold pool to the south of the vortex from the surface through 850 hPa, leading to weakening of the low-level convergence associated with the cold pool. The veering and weakening low-level jet may also be contributing to this weakening low-level convergence. The simulated

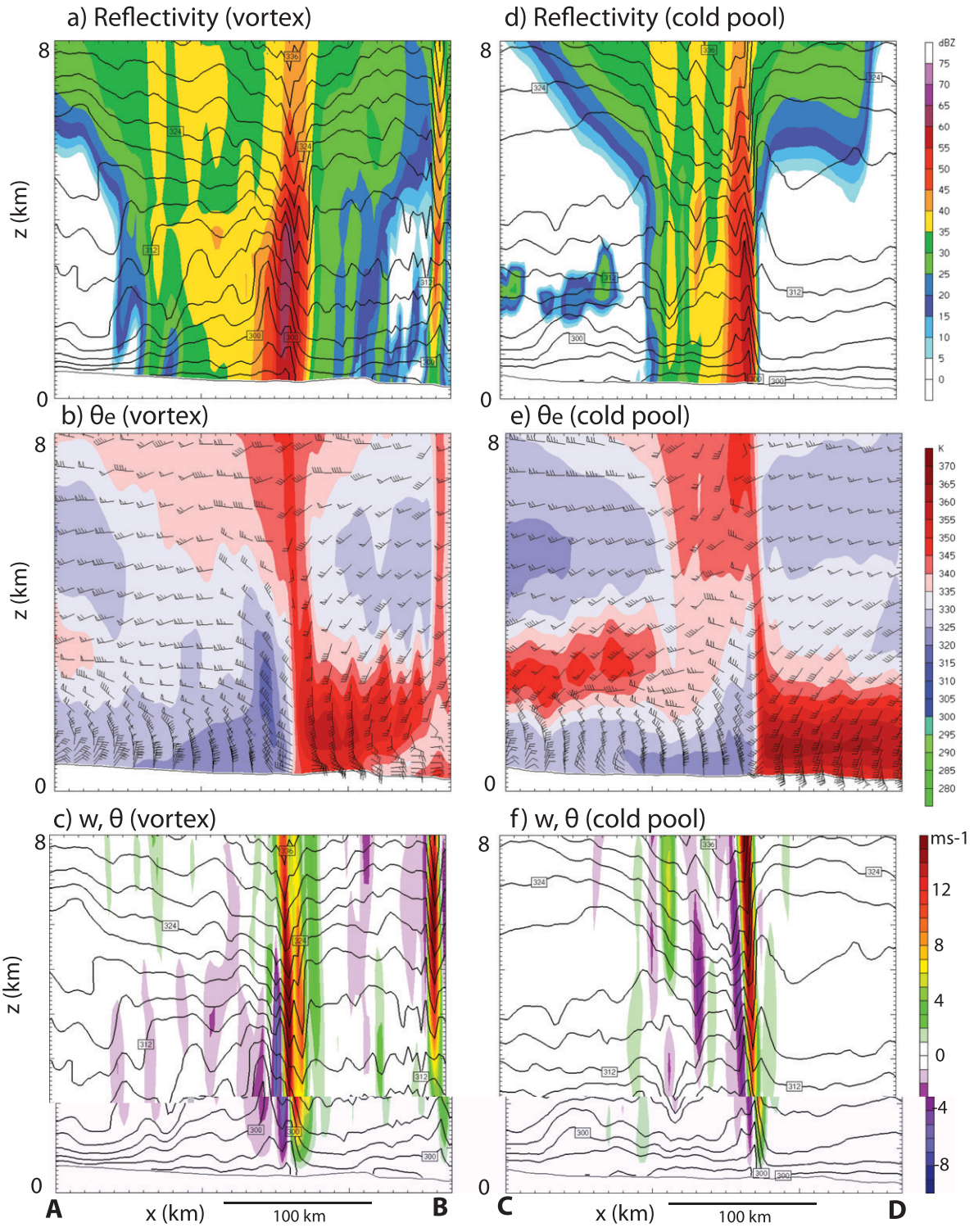

FIG. 12. East–west vertical cross sections at 0900 UTC 8 May 2009 of (a),(d) derived reflectivity (dBZ, shaded) and potential temperature (K, contoured), (b),(e) equivalent potential temperature (K, shaded) and winds (barbs, kt), and (c),(f) vertical velocity (m s^{-1}, shaded) and potential temperature (K, contoured) through the vortex (line AB in Fig. 7a) and cold pool (line CD in Fig. 7a), respectively. The east–west length of the cross sections is 270 km.

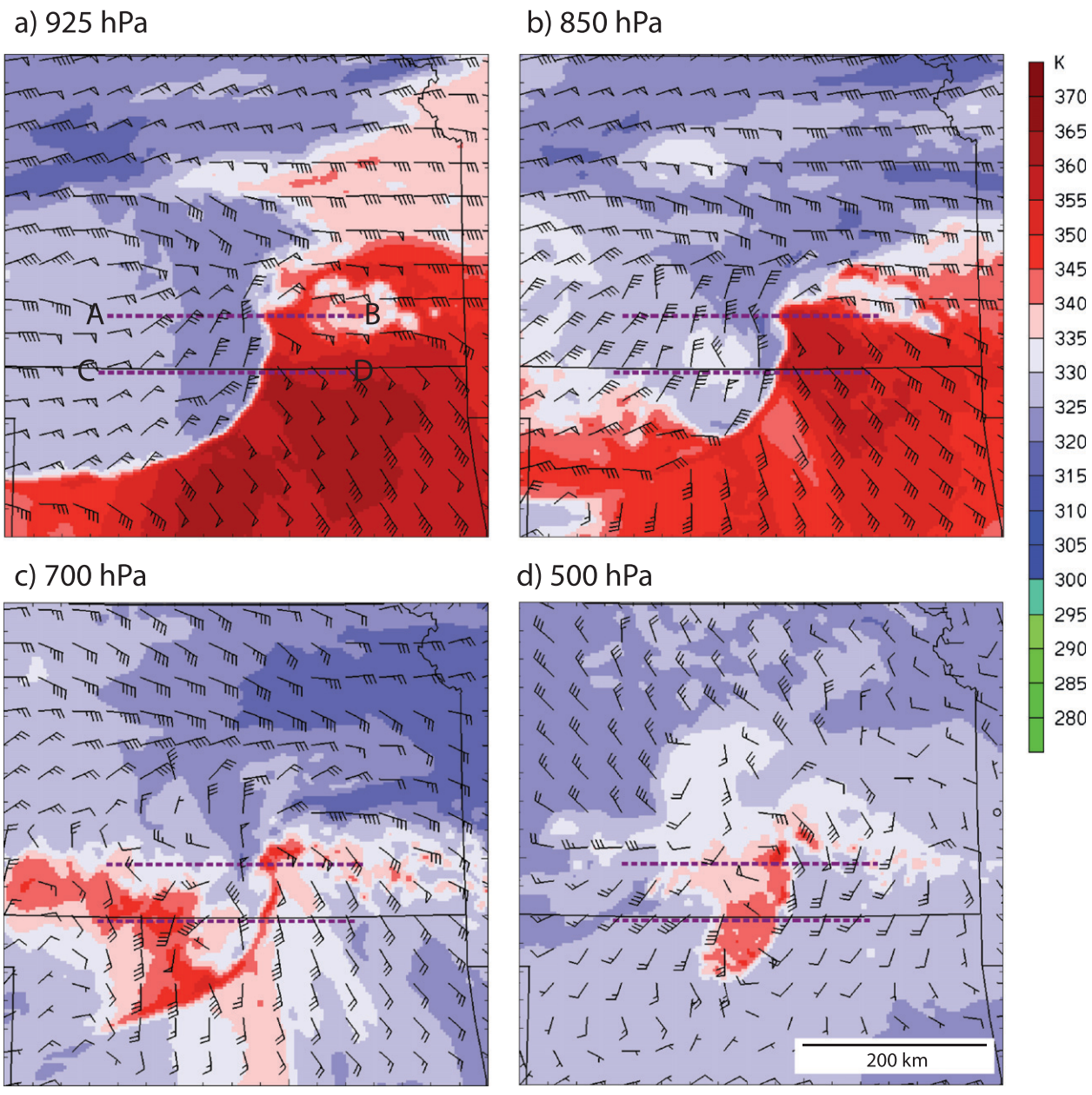

FIG. 13. Equivalent potential temperature (K, shaded) and storm-relative winds (barbs, kt) at 0900 UTC 8 May at (a) 925, (b) 850, (c) 700, and (d) 500 hPa, as in Fig. 8. Storm-relative winds are calculated using a 40-kt average eastward system propagation speed.

convective system (and associated mesoscale vortex) continues to weaken (not shown) as it propagates east-northeastward into an environment of increasingly weaker MUCAPE and vertical wind shear.

5. Further analyses and discussion

a. Vorticity evolution

The existence of such an intense vortex extending from the surface to the upper troposphere certainly represents one of the notable attributes of the present convective system. Although a detailed analysis of the source of this vorticity (and circulation) is outside the intended scope of the present paper (a companion study presenting a more complete vorticity and circulation analysis is forthcoming), it is still useful to describe the evolution of the vorticity field in more detail, to help further clarify the system's unique structural attributes and to help motivate future research directions.

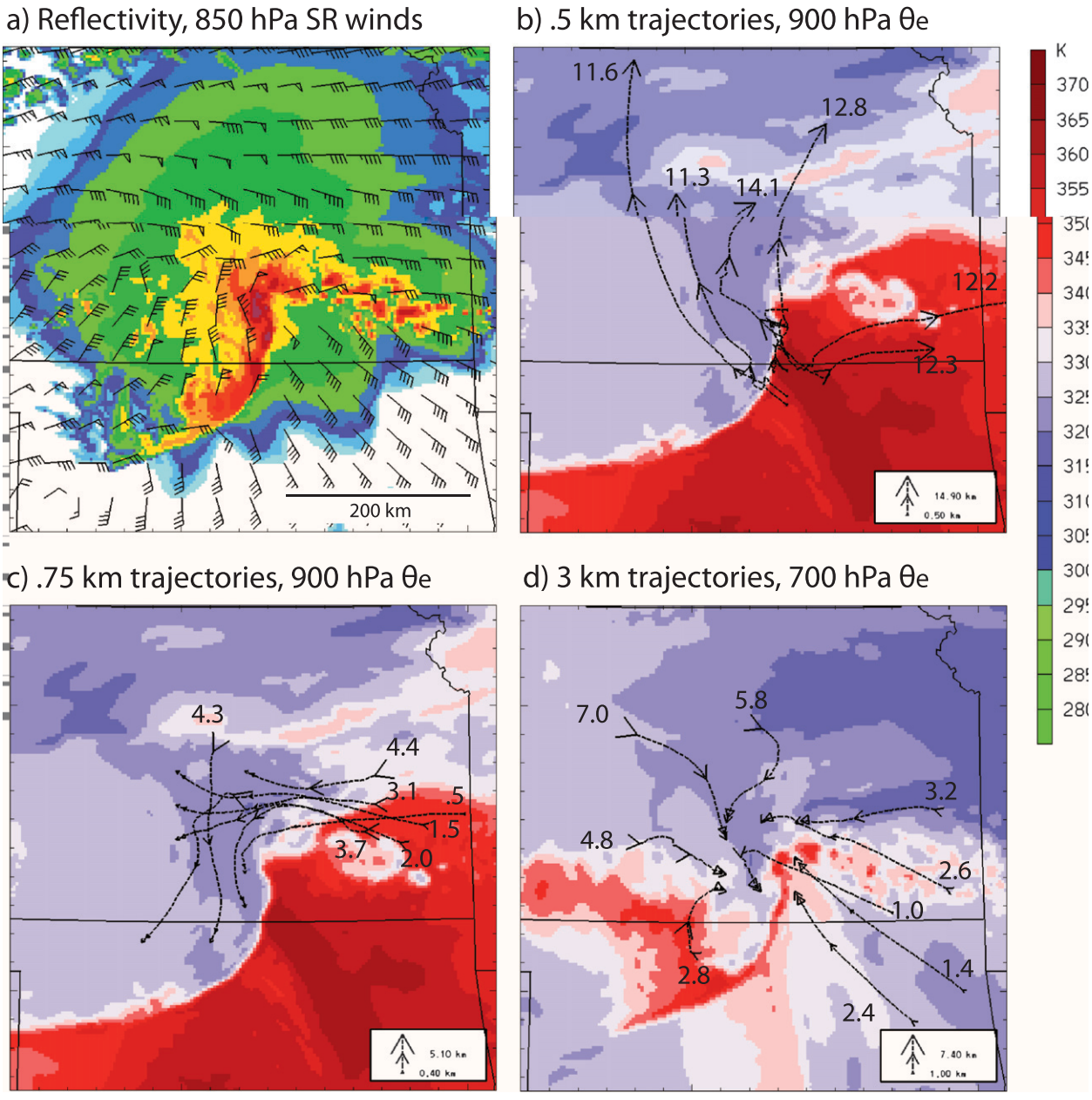

FIG. 14. Column maximum derived reflectivity (dBZ) and storm-relative flow at 850 hPa (kt) at 0900 UTC, (b) forward trajectories originating at 0.5 km AGL within the environment ahead of the convective line, (c) backward trajectories originating at 0.75 km within the system cold pool, and (d) backward trajectories originating at 3 km, surrounding the northernmost convective cell and associated mesovortex, all initiated at 0900 UTC. Trajectories are calculated over a 3-h time period. For the backward (forwards) trajectories, the height of origin (final height) for the trajectory (km) is included at the beginning (end) of each trajectory. The θ_e is shaded in (b),(c) at 925 and (d) at 700 hPa. Only a 510 km × 510 km portion of the full domain is shown.

To begin, a review of the larger-scale upper-tropospheric conditions associated with this system (e.g., 500 hPa and above; Figs. 5, 6) suggests that there was no obvious source of preexisting cyclonic vertical vorticity (or potential vorticity) to contribute to the development of the simulated mesovortex. Indeed, the system clearly develops on the anticyclonic shear side of an upper-level jet that was situated farther to the north. At lower levels, however, the system develops just to the east of a low- to midtroposphere trough and associated low-level jet, and somewhat north of an east–west surface boundary. All of these features exhibit weak cyclonic vertical vorticity that could conceivably contribute to the spinup of a mesovortex. However, the low- to midtropospheric

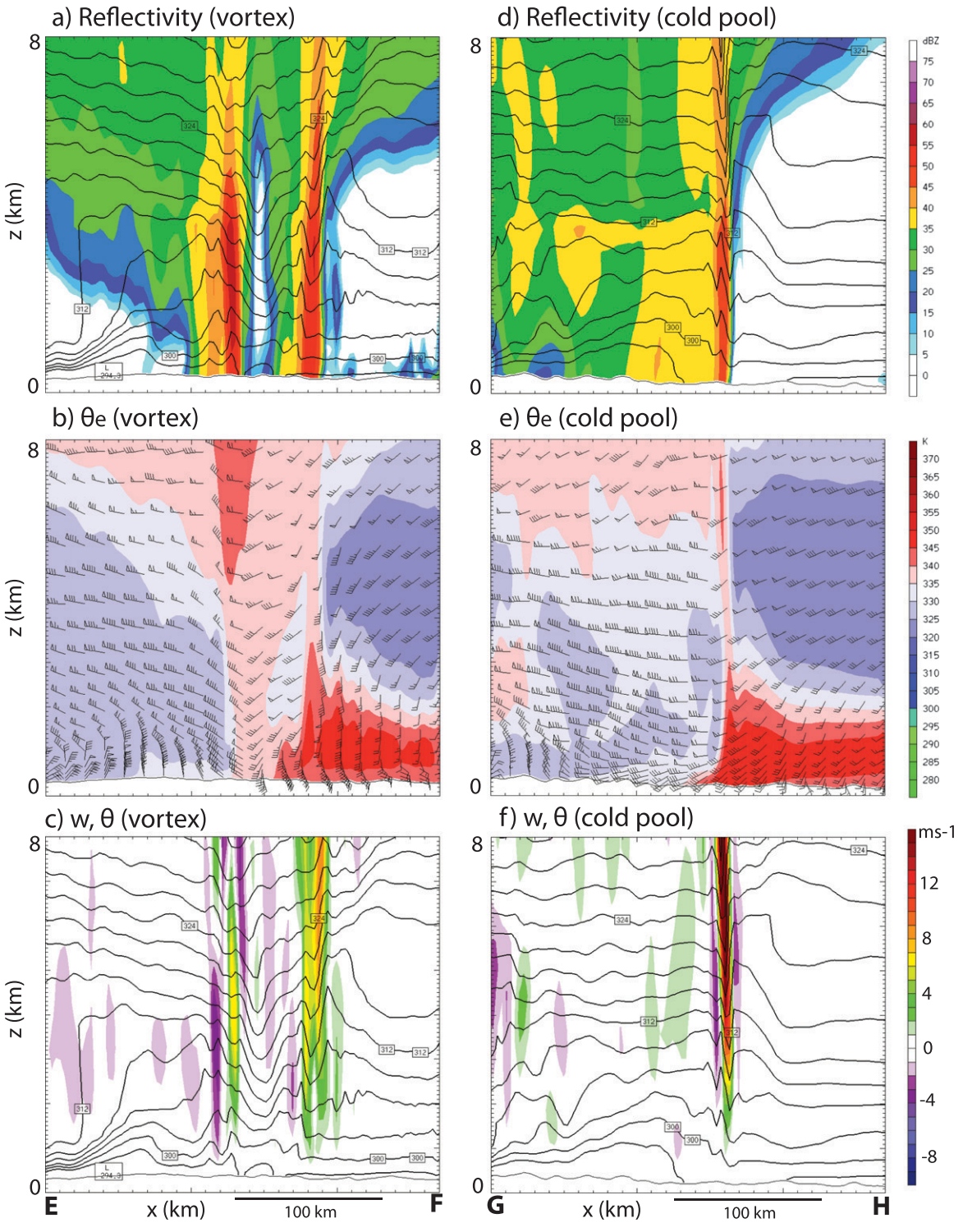

FIG. 15. East–west vertical cross sections at 1300 UTC 8 May 2009 of (a),(d) derived reflectivity (dBZ, shaded) and potential temperature (K, contoured), (b),(e) equivalent potential temperature (K, shaded) and wind (barbs, kt), and (c),(f) vertical velocity (m s^{-1}, shaded) and potential temperature (K; contoured) through the vortex (line EF in Fig. 7e, etc.) and cold pool (line GH in Fig. 7e, etc.), respectively. The east–west length of the cross sections is 270 km.

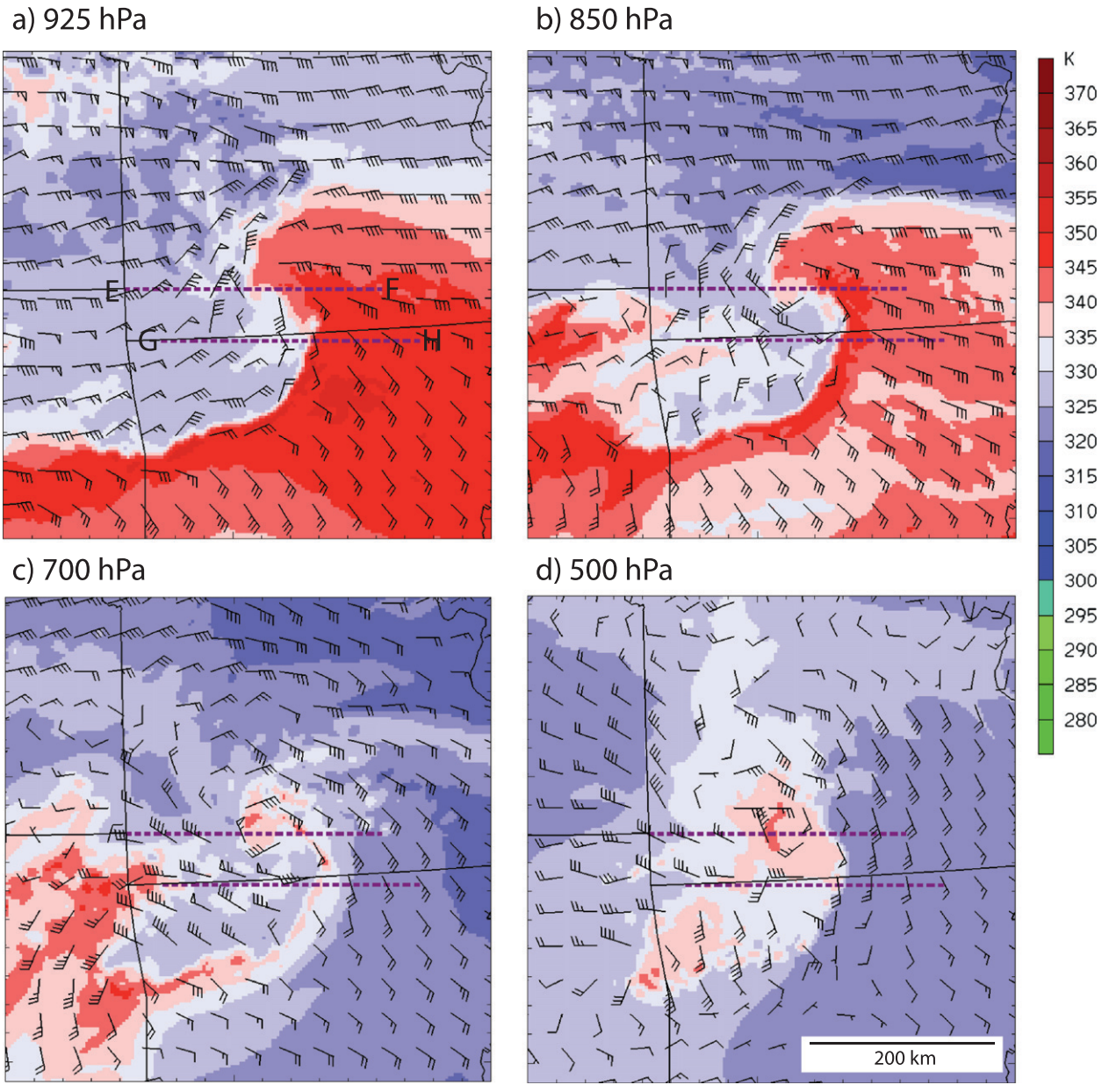

FIG. 16. Equivalent potential temperature (K, shaded) and storm-relative wind barbs (kt) at 1300 UTC at (a) 925, (b) 850, (c) 700, and (d) 500 hPa on 8 May 2009, as in Fig. 13.

cyclonic vorticity associated with the incipient modeled convective system appears to be generated significantly north of these preexisting features, with back trajectories from the incipient bookend vortex (not shown) suggesting no obvious connection. Additionally, the most intense phase of the mesovortex occurs quite far to the east of these features, in an environment with little evident background vertical vorticity.

A more detailed picture of the evolution of the vorticity field is presented in Fig. 18. By 0900 UTC (Fig. 18a), the flow field is characterized by a band of strong cyclonic vertical vorticity that extends southward from the northern end of the system, along and westward of the leading-line updraft. Some enhanced cyclonic vertical vorticity also extends eastward from the northern terminus along and north of the preexisting east–west boundary, associated with more isolated updraft features and their associated vertical vorticity couplets. The strongest positive vertical vorticity as well as the strongest updraft, however, are found near the intersection between

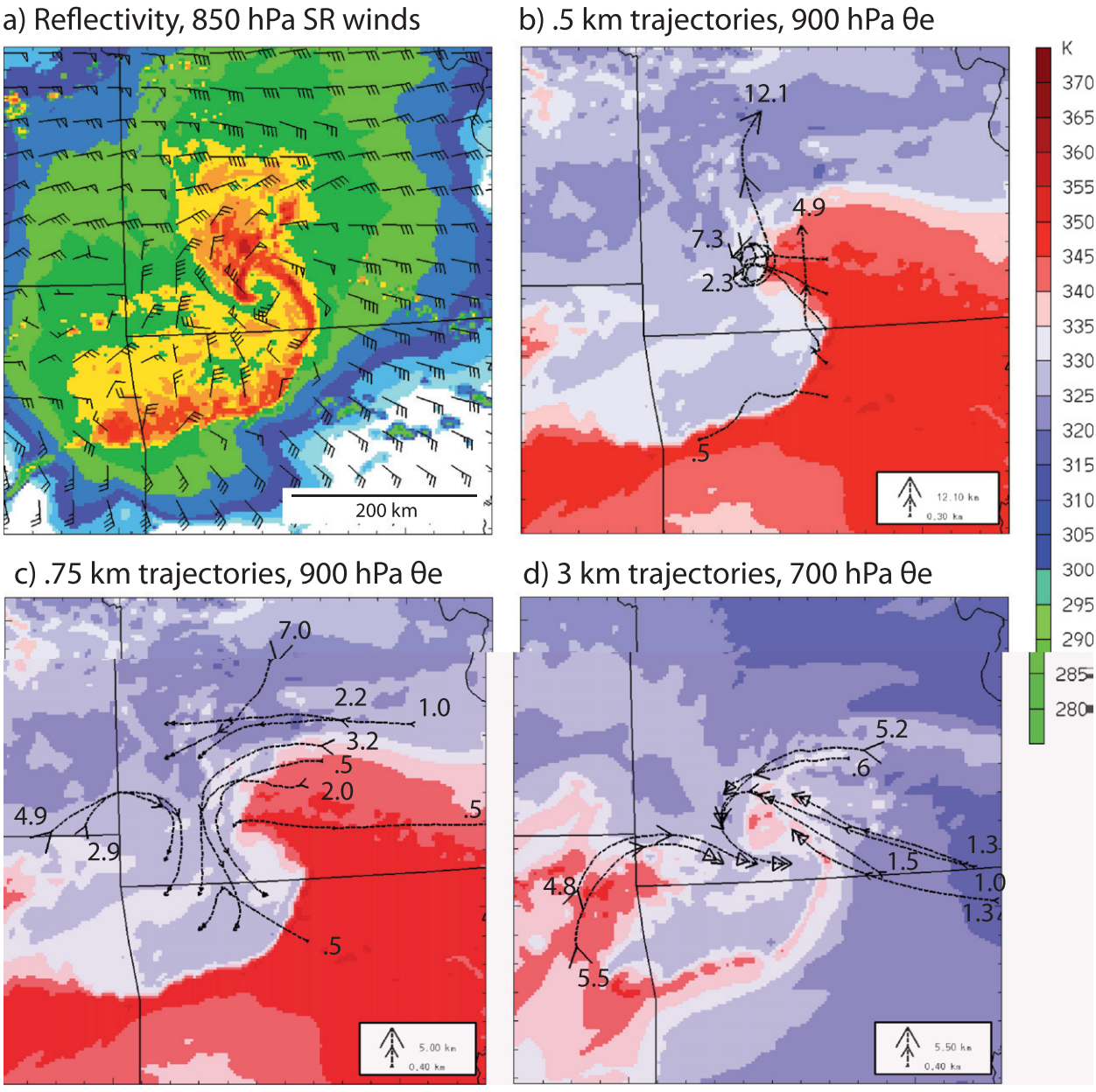

FIG. 17. Column maximum derived reflectivity, storm-relative flow, and trajectories, as in Fig. 14, at 1300 UTC.

this boundary and the bow-shaped system. Regions of significant anticyclonic vertical vorticity are found rearward of the primary bow feature in the cold air and are associated with weaker downdrafts. Weaker anticyclonic vertical vorticity is also evident on the north side of the system. East–west vertical cross sections through the head of the bow (Fig. 19a) show that the cyclonic vertical vorticity extends from near the surface to 8 km AGL (and above) and is collocated with positive vertical motions, especially at midlevels (Fig. 19b). Calculations of the linear correlation coefficient between the vertical vorticity and positive vertical velocity (not shown) indicate magnitudes of 0.5–0.8 at midlevels at the northern end of the system during much of this early phase of system evolution, consistent with the magnitudes generally associated with supercell storms (e.g., Weisman and Klemp 1984; Weisman and Rotunno 2000). A large region of anticyclonic vertical vorticity associated with weak downdrafts remains situated rearward of the primary bow. This vertical vorticity configuration remains intact through 1100 UTC (Fig. 18b) with the eastward-extending wing becoming more elongated and

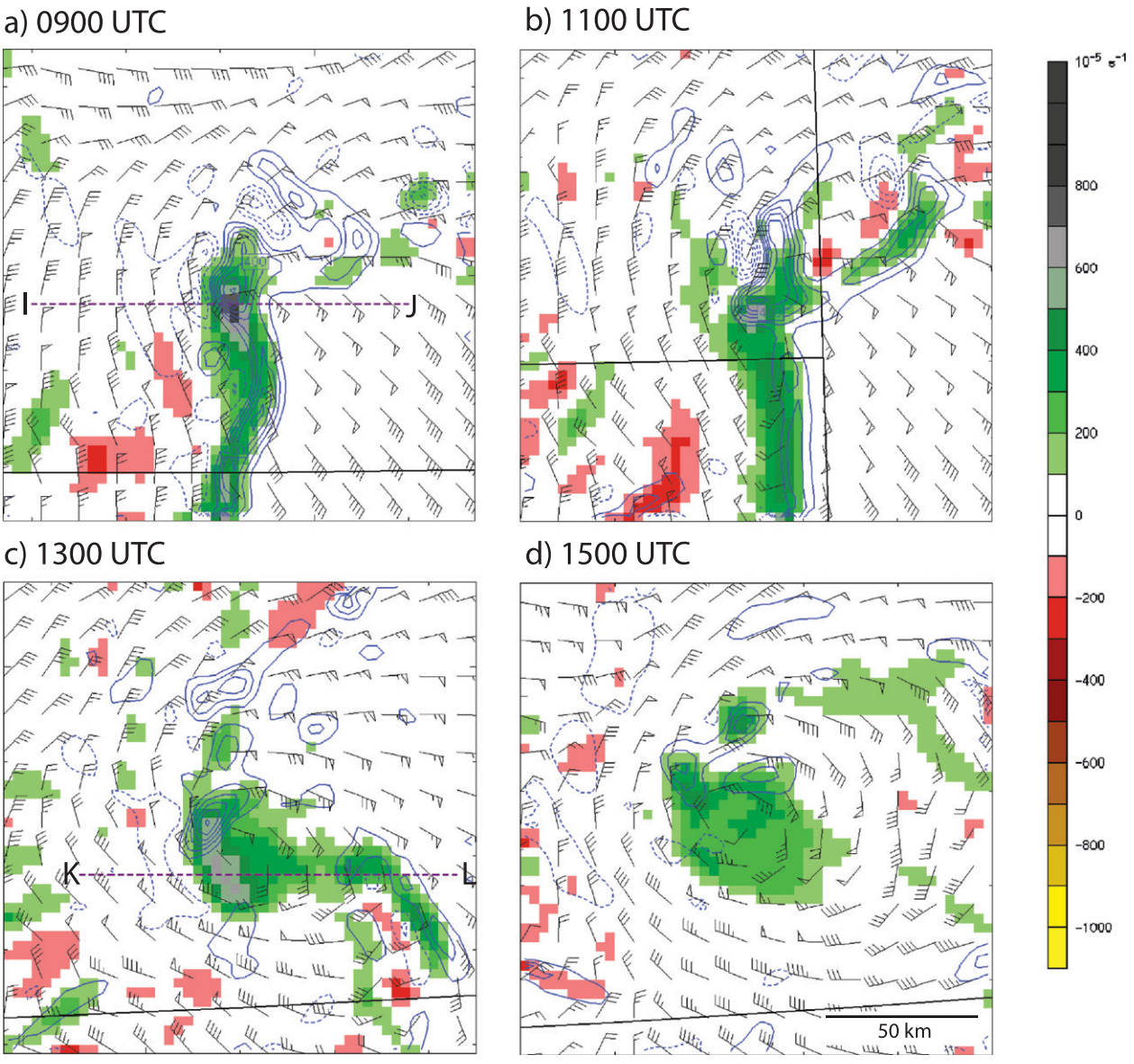

FIG. 18. Vertical vorticity ($\times 10^{-5}$, shaded), vertical velocity (contoured every 1 m s^{-1}) and storm-relative wind barbs (kt) at 850 hPa at (a) 0900, (b) 1100, (c) 1300, and (d) 1500 UTC 8 May 2009, from the 3-km WRF-ARW real-time forecast initialized at 1200 UTC 7 May 2009. Winds (barb) are spaced every four grid points (12 km). Only a 150 km × 150 km portion of the full domain is shown.

continuous. This basic vertical vorticity pattern becomes established by 0600 UTC (not shown), suggesting that this configuration of vertical vorticity may represent a robust characteristic of convective systems evolving within the present environment.

During the comma echo phase (Figs. 18c,d), the primary bow-shaped band of positive vertical vorticity consolidates at the northern end of the system as the leading-line updraft surges eastward and northward around the new mesovortex. The leading-line updraft also weakens and becomes less collocated with the region of positive vertical vorticity. The region of more isolated convection originally extending to the east of the primary mesovortex, however, maintains its intensity as it rotates cyclonically around the northern end of the mesovortex. An east–west vertical cross section through the core mesovortex at 1300 UTC (Fig. 19c) shows that the vertical vorticity feature remains deep but is broader than earlier and now appears to be strongest at the surface. However, much of the primary vortex is now associated with predominantly negative vertical velocities (Fig. 19d), especially in the upper

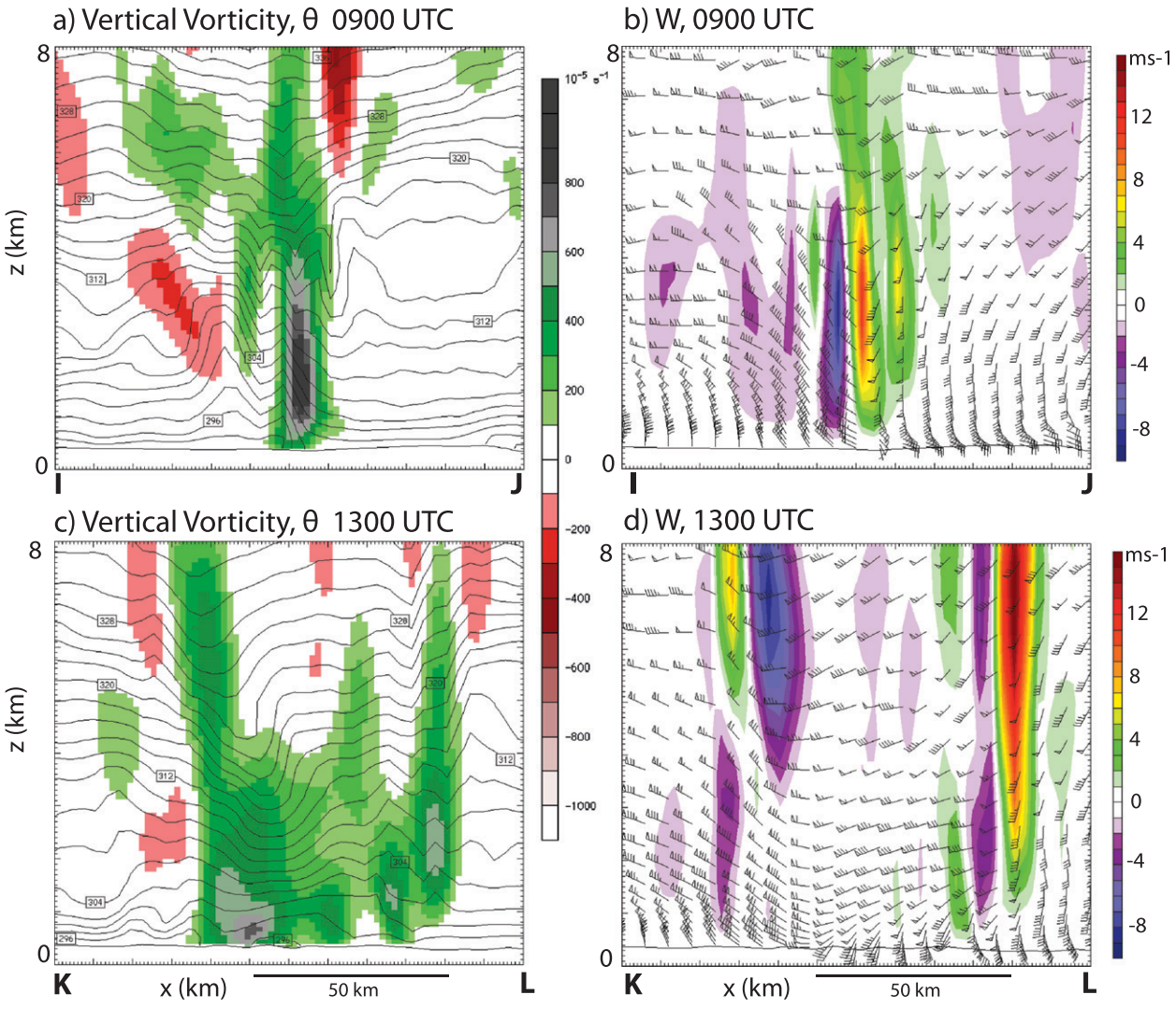

FIG. 19. East–west vertical cross sections through the northern vortex core of (a),(c) vertical vorticity ($\times 10^{-5}$, shaded) and potential temperature (K, contoured), and (b),(d) vertical velocity (m s^{-1}, shaded) and winds (barbs, kt), at 0900 and 1300 UTC, along lines IJ and KL, as located in Figs. 18a and 18c, respectively, from the 3-km WRF-ARW real-time forecast initialized at 1200 UTC 7 May 2009. The east–west length of the cross sections is 120 km.

troposphere. By 1500 UTC (Fig. 18d), the mesovortex has expanded further in scale but has now begun to weaken a bit in terms of maximum vertical vorticity. This weakening trend subsequently continues over the following several hours (not shown).

Past idealized modeling studies clearly show how intense mesoscale vortices can be generated within convective systems as a result of convective-scale and mesoscale-scale processes, via the tilting of ambient or system-generated horizontal vorticity and subsequent stretching of the resulting relative and planetary vertical vorticity (e.g., Skamarock et al. 1994; Davis and Weisman 1994; Weisman and Davis 1998; Cram et al. 2002). However, the existence of a deep strip of cyclonic vertical vorticity extending along and behind the leading-line convection during much of the system's lifetime (e.g., Figs. 18a–d, 19a,c) appears quite different from these past studies, whereby such mesoscale vortices have either been limited to the ends of the system (e.g., bookend or line-end vortices), or appear as more isolated low-level vorticity features along the leading line. Wheatley and Trapp (2008) do describe the development of a continuous shallow strip of cyclonic vorticity (vortex sheet) along the leading edge of a simulated severe wintertime bow-echo system. However, the deeper, stronger mesovortices remained relatively isolated along the leading line, appearing to develop upward in response to stretching by locally intense updrafts.

The apparent differing vertical vorticity evolution for the present case may be related to the existence of a significant, line-parallel component of lower-troposphere shear in the system's environment [associated with the low-level jet; e.g., Coniglio et al. (2012)], as compared to the simple unidirectional, line-perpendicular vertical wind shear profiles specified in many of the previous, more idealized studies. In particular, such line-parallel low-level shear can translate into system-relative streamwise vorticity that can be ingested by the updrafts within the line, thereby potentially producing a more supercellular character to such updrafts (e.g., Davies-Jones 1984; Weisman and Rotunno 2000). Indeed, it has already been noted that the northernmost updraft cell in the present simulation is strongly correlated with strong cyclonic vertical vorticity through much of the simulation, as would be expected within a supercell storm. Such line-parallel shear was also identified by Wheatley and Trapp (2008) as a possible contributor to the development of the shallow strip of cyclonic vorticity noted in their case.

The character of the low-level shear for the present case is further clarified in Fig. 20, which presents horizontal vorticity vectors along with storm-relative wind vectors at 0900 and 1300 UTC. At 0900 UTC, a broad region of positive streamwise vorticity (e.g., storm-relative velocity vectors parallel to the horizontal vorticity vectors) is evident at 900 hPa throughout the warm sector of the system (Fig. 20a). The northwestward pointing horizontal vorticity vectors at this level correspond directly with the strong low-level northeastward-pointing vertical wind shear associated with the low-level jet. Some positive streamwise vorticity is also evident along the eastward-extending baroclinic zone at 800 hPa (Fig. 20b). Both of these sources of streamwise vorticity appear to converge into the persistent northern cyclonic cell noted above. At 1300 UTC (Fig. 20c), significant positive streamwise vorticity is still evident at 900 hPa in the warm sector of the system, and still appears to converge into the northernmost cell, which has now rotated around to the northwest side of the mesovortex. Streamwise vorticity is also now evident at 900 hPa within the cold pool, feeding around the eastern side of the mesovortex. Some weaker streamwise vorticity can also still be identified at 800 hPa along the preexisting baroclinic zone, which has now rotated around to the north side from the mesovortex (Fig. 20d). All in all, this preliminary analysis clearly suggests a possible role for low-level environmental streamwise vorticity in the evolution of the northern cell and associated mesovortex for this case. A more quantitative appraisal of all the possible sources of vertical vorticity for the present case is on going.

b. Cold-pool evolution

Cold pools have been identified as a key component of convective system structure and evolution, having a strong influence on leading-line updraft strength, depth, and orientation. Generally, simulated quasi-two-dimensional convective systems exhibit an overall downshear, upright, or upshear-tilted structure dependent on the strength of the cold pool relative to the strength of the ambient vertical wind shear (e.g., Rotunno et al. 1988; Weisman et al. 1988; Weisman and Rotunno 2004; Bryan et al. 2006). These studies consistently suggest that the strongest, most upright updrafts along the leading edge of a convectively generated cold pool occur when the cold pool spreads into an environment of moderate-to-strong low- to mid-tropospheric vertical wind shear [typically $>$(15–20) m s^{-1} over the 0–5-km AGL layer] oriented perpendicular to the spreading cold pool.

Weisman (1992, 1993) expanded these results to more three-dimensional bow-shaped systems, considering the additional role of rear-inflow jets and bookend vortices in the evolution of such systems. In particular, the development of a rear-inflow jet and bookend (or line end) vortices characteristically occurs when a convective system develops an upshear-tilted system structure. Subsequently, if the rear-inflow jet remains elevated to near the leading edge of the system, an upright, leading-line updraft may be reestablished, thereby helping to maintain overall system strength. An elevated rear-inflow jet is favored for environments in which the negative buoyancy within the convectively generated cold pool is comparable to or weaker than the positive buoyancy associated with the front-to-rear updraft current aloft. The production of an elevated rear-inflow jet in the present case seems consistent with this result in that the system evolves in an environment of large MUCAPE, which contributes to a highly buoyant front-to-rear updraft current but only a modestly strong convectively generated cold pool.

An intriguing aspect of the present case is the notable weakening of the cold pool during the comma-echo phase of the system, suggesting that the cold pool is not playing a dominant role in this phase of the evolution. Indeed, both in the observations (Fig. 3) and the simulation (Fig. 9), the maximum potential temperature deficit within the cold pool decreases from 6 to 8 K during the systems early evolution to only 2–4 K once the system has occluded. The cold-pool strength can also be measured by the theoretical speed of propagation of a density current; for example,

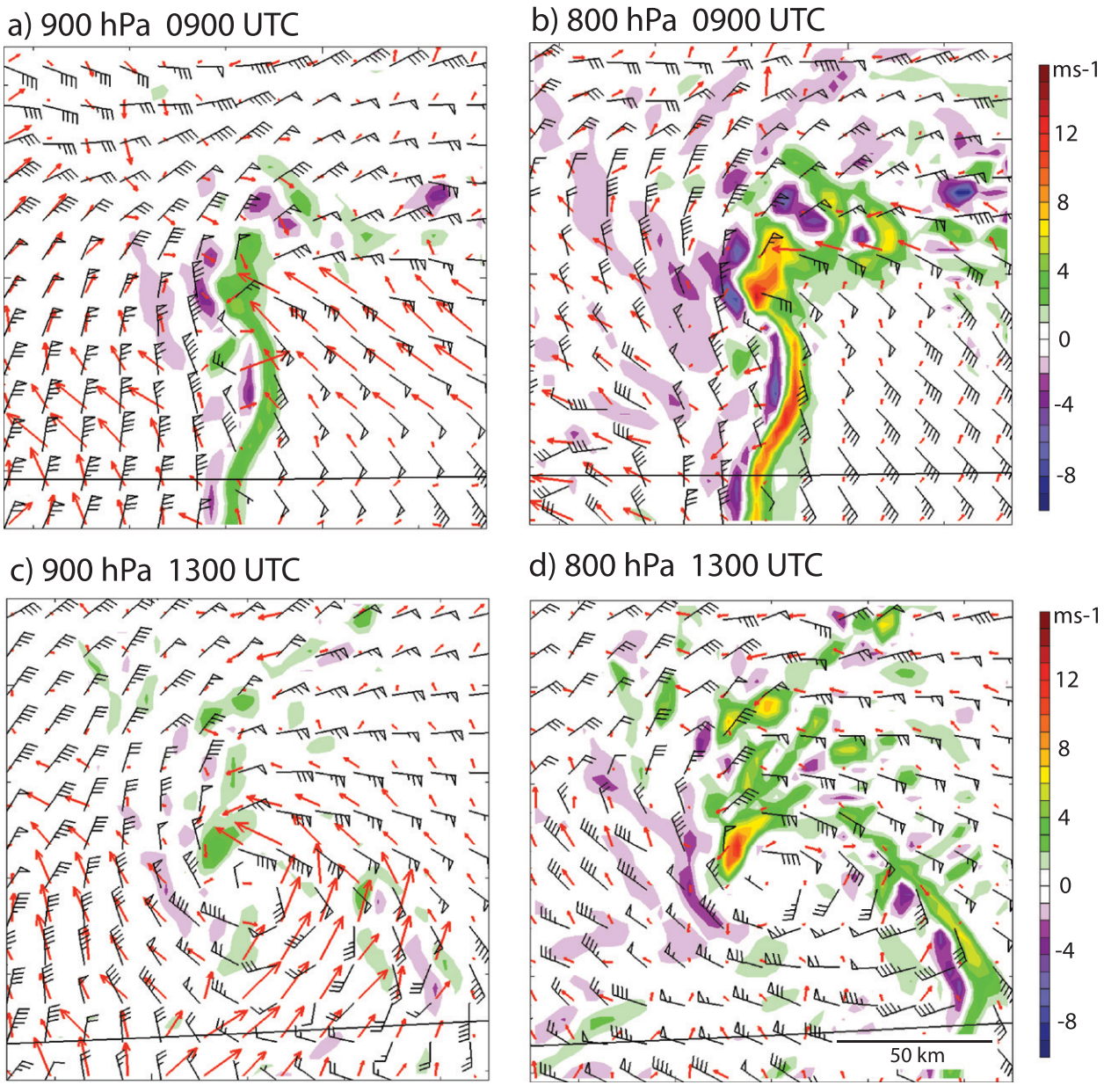

FIG. 20. Horizontal vorticity (vectors), storm-relative flow (wind barbs), and vertical velocity (m s^{-1}, shaded) at (a),(b) 0900 and (c),(d) 1300 UTC, plotted at 900 and 800 hPa, respectively. Storm-relative winds are calculated using a 40-kt average eastward system propagation speed. Vectors and wind barbs are spaced every 12 grid points (36 km). Horizontal vorticity vectors are scaled at 3500 s^{-1} per a 12-gridpoint interval. Only a 510 km × 510 km portion of the full domain is shown.

$$C^2 = 2\int_0^H (-B)\,dz, \tag{1}$$

where H is the depth of the cold pool and buoyancy B is given by

$$B \equiv g\left[\frac{\theta'}{\overline{\theta}} + 0.61(q_v - \overline{q}_v) - q_c - q_r\right], \tag{2}$$

where $\overline{\theta}$ is the mean environmental potential temperature, θ' is the perturbation potential temperature, and q_v, q_c and q_r are the mixing ratios of water vapor, cloud water, and rainwater, respectively. A mean environmental state for the present simulation is specified by averaging the potential temperature and water vapor mixing ratio over a 30 × 30 km^2 box centered approximately 35 km ahead of the apex (leading edge) of the

cold pool. A representative C is then calculated from (1) by averaging the buoyancy 10–20 km rearward and 30 km north and south of this apex at each time. Cold-pool depth (H) is defined herein as the altitude at which the area-averaged buoyancy in the cold pool becomes positive. This altitude is found at approximately 3750 m AGL at 0900 UTC and at approximately 3400 m AGL at 1300 UTC. Using this methodology, C is estimated to be 43 m s^{-1} at 0900 UTC, decreasing to 24 m s^{-1} at 1300 UTC. Water-loading contributions to the buoyancy are small at both times (not shown).

The overall balance between the cold-pool-generated circulation and the ambient vertical wind shear can be expressed by the ratio $C/\Delta u$, where Δu represents the line-perpendicular vertical wind shear over the depth of the cold pool. Generally, magnitudes of $C/\Delta u$ much less than 1, about 1, and much greater than 1 are conducive to convective systems that are downshear tilted, upright, and upshear tilted, respectively (Rotunno et al. 1988; Weisman and Rotunno 2004). The environmental Δu at 0900 UTC (estimated from Fig. 21a, taken 10–30 km ahead of the cold pool) ranges between 15 and 25 m s^{-1} over the lowest 3.75 km, yielding a $C/\Delta u$ of 1.7–2.9. Based on the aforementioned modeling studies, such a $C/\Delta u$ would be consistent with an upshear-tilted system, as would be expected for a system that develops a strong rear-inflow jet. By 1300 UTC, the representative environmental Δu has been reduced to 10–15 m s^{-1} over the cold-pool depth (as estimated from Fig. 21b), yielding a range of $C/\Delta u$ of 1.6–2.4, which would continue to support an upshear-tilted system-scale structure.

Following Weisman (1992), the role of the elevated rear-inflow jet can be incorporated into this balance condition by considering a modified ratio $C_j/\Delta u$ where $C_j = (C^2 - \Delta u_j^2)^{1/2}$, and where Δu_j represents the wind magnitude difference between the surface and the height of the elevated rear-inflow jet within the cold pool. From Fig. 21, averaging over a 10–20-km region rearward of the leading edge of the cold pool Δu_j is estimated to be 25 m s^{-1} at 0900 UTC, increasing to about 30 m s^{-1} at 1300 UTC. Thus, $C_j/\Delta u$ is estimated to be between 1.4 and 2.3 at 0900 UTC, indicating a more balanced state when one includes the effects of the elevated rear-inflow jet. However, by 1300 UTC, Δu_j is actually greater than C, resulting in $C_j/\Delta u < 0$, which is outside the range considered in Weisman (1992). In point of fact, the convective line at this later stage appears more elevated in character rather than cold pool driven, somewhat akin to a nocturnal convective system persisting in the presence of a stable boundary layer (e.g., Parker 2008). Indeed, as noted above, many of the near-surface inflow parcels at this time pass under or through the leading line updraft and into the cold pool, as opposed to earlier in the simulation when such parcels were all lifted into deep updraft cores. Similarly, one might argue that the flow-through character of the surface winds through the cold pool at this later time (Fig. 21b) is closer to descriptions of a bore than a classic density current (e.g., Parker 2008). In any event, the existence of an elevated rear-inflow jet, which acts like a deep barrier that can effectively lift storm-relative inflow parcels to above the level of free convection (e.g., Weisman 1992), may be all that is needed to maintain such convective systems.

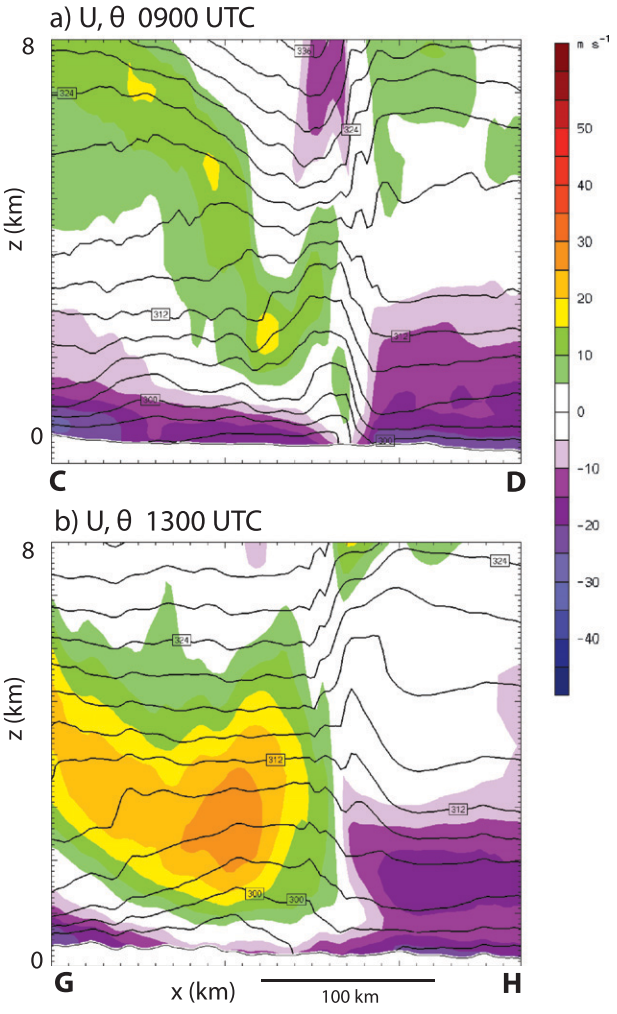

FIG. 21. East–west vertical cross sections through the cold pool of the storm-relative U component of wind (m s^{-1}, shaded) and potential temperature (K, contoured) at (a) 0900 and (b) 1300 UTC, along lines CD and GH, as located in Figs. 7a and 7e, respectively. Cross sections are averaged in the north–south direction over a 60-km region centered on the nominal cross-section location. A storm motion of 20 m s^{-1} has been subtracted from the U wind component. The east–west length of the cross sections is 270 km.

6. Summary and discussion

In the foregoing, we present an analysis of a 3-km real-time explicit convective simulation of an unusually intense bow echo and associated mesoscale vortex that produced an extensive swath of high winds across Kansas, southern Missouri, and southern Illinois on 8 May 2009. In both the simulation and reality, the system organized first as elevated convection in west-central Kansas north of a weak east-west lower-tropospheric boundary and at the nose of an intensifying low-level jet. The simulated system quickly organized into a north–south-oriented bow echo (the observed system took longer to do so) with a strong, cyclonically rotating convective cell at its northern end at the intersection of the bow echo and the preexisting east–west midtropospheric baroclinic zone. During this phase of its evolution, strong surface winds were produced along the entire extent of the surface cold pool, as is often observed with derecho events, with the strongest surface winds occurring in association with a northern cyclonic bookend vortex. This configuration lasted for several hours as the system moved east along this zone in an environment of high MUCAPE and strong tropospheric vertical wind shear. Once the system started to progress east of the low-level jet and into an environment of weaker MUCAPE and vertical wind shear, it continued to grow in scale and intensity, producing a pronounced comma-shaped echo in association with an intense, 100-km-wide warm-core mesovortex that extended from the surface to above 500 hPa. During this phase, the strongest surface winds were associated with this mesovortex at the head of the comma well behind the system-scale gust front. The simulated system eventually weakened as it continued eastward into a less unstable environment.

The basic vertical vorticity structure of the simulated system became established very early in its life cycle and was characterized by a deep strip of cyclonic vertical vorticity extending along and behind the leading line of convection. Cyclonic vertical vorticity and vertical velocity were nearly collocated at the northern end of the system where the convection intersected the preexisting east–west boundary. During the transition to a comma echo, this strip of cyclonic vertical vorticity consolidates into a more symmetric vortex situated on the southern flank of the northernmost cell while becoming collocated primarily with downdraft at low-to-midtropospheric levels.

The similarity between the evolution of the warm-core mesovortex in the present case and the occlusion–seclusion process for synoptic-scale cyclones (e.g., Shapiro and Keyser 1990; Schultz and Vaughan 2011) seems particularly intriguing. Following Schultz and Vaughan (2011), occlusion can be defined as the process by which warm-sector air is separated from a low center through the wrap-up of the thermal wave around the cyclone, often accompanied by the continuing deepening of the parent cyclone. For the present case, the convective cold pool is analogous to the synoptic-scale cold front while the midtropospheric baroclinic region serves as a warm front. The occlusion-like process proceeds as the northern bookend vortex at the intersection of the cold pool and eastward-extending baroclinic zone intensifies, wrapping warm, high-θ_e air westward around the mesovortex. Subsequently, the mesovortex and associated surface mesolow continue to intensify as they become increasingly separated from the warm sector to the southeast, in the process developing a classic warm-core structure that is enhanced by midtropospheric descending motion at its center. Indeed, the present case even exhibits similar basic airstreams (trajectories) to an occluding cyclone, including a cyclonically turning warm conveyor belt, cold conveyor belt, and descending dry intrusion (rear-inflow jet) (e.g., Figs. 14, 17). However, one significant departure from the synoptic-scale conceptual models for the present case is the lack of upper-level forcing in the form of a preexisting upper-tropospheric potential vorticity anomaly or the like.

Another intriguing aspect of the system's evolution was the observed and simulated weakening of the low-level cold pool over time. A strong surface cold pool has generally been considered one of the primary ingredients for the production of strong surface winds within such systems. However, during the occlusion-like phase, the cold pool was noticeably weaker, with the leading-line convection taking on a more elevated character. Some of the weakening perhaps can simply be attributed to cooler surface temperatures ahead of the system, although this is not nearly enough to explain the larger changes within the convective cold pool. The derecho also is moving into an environment with progressively weaker MUCAPE, which is generally associated with weaker downdraft potential. Additionally, by the time the system appears to occlude, the environment of the mesovortex has evolved to a nearly moist-neutral state, thereby also reducing the potential for further cold-pool production. It is certainly common for cold pools to weaken during the mature and decaying stages of convective systems (e.g., Engerer et al. 2008), but what seems unique in the present case is that the weakening of the cold pool coincides with a strengthening of the surface winds associated with the mesoscale vortex well behind the leading edge of the cold pool.

Idealized simulations of such convective systems produce strong bookend or line-end-type mesovortices at midtropospheric levels, but such mesovortices generally

do not extend down to the surface [except for the generally smaller-scale leading-line mesovortices described by Weisman and Trapp (2003) and Trapp and Weisman (2003)]. However, these past studies considered environments that produced relatively strong surface cold pools, potentially limiting the ability of a midtropospheric vortex to extend to the surface, due to the presence of low-level diverging flow. In cases where these vortices evolve into an MCV, a weak [$\Delta p \sim$(1–2) hPa] surface reflection is often more evident the next day, after the original convection and associated cold pool have weakened or dissipated (e.g., Davis and Galarneau 2009). More generally, the production of a moist-neutral environment with weak or absent cold pools is believed to be a key step for the eventual intensification of tropical cyclones (e.g., Montgomery and Farrell 1993). Thus, the relative role of a weakening cold pool in the development of the resulting unusually intense surface mesolow in the present case warrants further study.

Many other aspects of the simulated system environment and evolution also seem noteworthy within the context of past studies. For instance, the role of the preexisting midtropospheric baroclinic zone and the low-level jet needs to be better established in terms of the preconditioning of the mesoscale environment to one favorable for such an intense event. Past studies have also suggested a more direct role for such boundaries–baroclinic zones in enhancing system severity, via the enhanced lifting and cyclonic vertical vorticity that are present near the boundary–bow echo intersection point and or the enhanced streamwise vorticity that can be ingested by the updrafts within the line, thereby producing a more supercellular character to such updrafts (e.g., Wheatley and Trapp 2008). The northernmost cell in the present simulation does exhibit a strong correlation between cyclonic vertical vorticity and positive vertical velocity, as would be expected within a supercell storm, and environmental streamwise horizontal vorticity was certainly evident at low levels in the warm sector of the system and along the preexisting baroclinic zone. However, the precise role of this streamwise vorticity in the development of the northern cyclonically rotating cell and eventual mesoscale vortex remains unclear. Furthermore, the primary mesovortex intensification phase seems to commence as the system moves into an environment of weakening shear and MUCAPE as it moves away from the low-level jet. Is this transition in environmental conditions critical to the observed change in system character? Finally, given the existence of the northern rotating cell in the simulation, this case may also offer insights into recent hypotheses related to tropical cyclogenesis, which have considered, for instance, the role of vortical hot towers (e.g., Hendricks et al. 2004) to help explain how convection can contribute to initial vortex spinup.

The 8 May 2009 derecho was certainly exceptional in its scale and intensity. However, as noted in the introduction, similar yet far less documented events have appeared in the literature and conference proceedings. It is hoped that this overview of the present ''surrogate'' simulation has motivated renewed interest in the intriguing dynamic character of such events. Forthcoming companion studies will offer a more detailed analysis of the vorticity and circulation generation mechanisms for this case as well as a more complete discussion of the forecast sensitivities.

Acknowledgments. We would like to acknowledge the significant help of Wei Wang and Kevin Manning, who supported the real-time forecasting exercise and supplied the many retrospective sensitivity forecasts for further evaluation. We have also benefited greatly from discussions and reviews of this manuscript by Rich Rotunno, Chris Davis, Stan Trier, and Mike Coniglio. The second author acknowledges the support of an NCAR Advanced Study Program postdoctoral fellowship through the duration of this work.

REFERENCES

Atkins, N. T., and M. S. Laurent, 2009: Bow echo mesovortices. Part I: Processes that influence their damaging potential. *Mon. Wea. Rev.,* **137,** 1497–1513.

——, J. M. Arnott, R. W. Przybylinski, R. A. Wolf, and B. D. Ketcham, 2004: Vortex structure and evolution within bow echoes. Part I: Single-Doppler and damage analysis of the 29 June 1998 derecho. *Mon. Wea. Rev.,* **132,** 2224–2242.

——, C. S. Bouchard, R. W. Przybylinski, R. J. Trapp, and G. Schmocker, 2005: Damaging surface wind mechanisms within the 10 June 2003 Saint Louis bow echo during BAMEX. *Mon. Wea. Rev.,* **133,** 2275–2296.

Bartels, D. L., and R. A. Maddox, 1991: Midlevel cyclonic vortices generated by mesoscale convective systems. *Mon. Wea. Rev.,* **119,** 104–118.

Bentley, M. L., and T. L. Mote, 1998: A climatology of derecho-producing mesoscale convective systems in the central and eastern United States, 1986-95. Part I: Temporal and spatial distribution. *Bull. Amer. Meteor. Soc.,* **79,** 2527–2540.

Bosart, L. F., and F. Sanders, 1981: The Johnstown flood of July 1977: A long-lived convective system. *J. Atmos. Sci.,* **38,** 1616–1642.

——, W. E. Bracken, A. Seimon, J. W. Cannon, K. D. Lapenta, and J. S. Quinlan, 1998: Large-scale conditions associated with the northwesterly flow intense derecho events of 14–15 July 1995 in the northeastern United States. Preprints, *19th Conf. on Severe Local Storms,* Minneapolis, MN, Amer. Meteor. Soc., 503–506.

Brandes, E. A., 1990: Evolution and structure of the 6–7 May 1985 mesoscale convective system and associated vortex. *Mon. Wea. Rev.,* **118,** 109–127.

Bryan, G. H., J. C. Kneivel, and M. D. Parker, 2006: A multimodel assessment of RKW theory's relevance to squall-line characteristics. *Mon. Wea. Rev.,* **134,** 2772–2792.

Cannon, J. W., K. D. Lapenta, J. S. Quinlan, L. F. Bosart, W. E. Bracken, and A. Seimon, 1998: Radar characteristics of the 15 July 1995 northeastern U.S. derecho. Preprints, *19th Conf. on Severe Local Storms,* Minneapolis, MN, Amer. Meteor. Soc., 440–443.

Chen, F., and J. Dudhia, 2001: Coupling an advanced land surface–hydrology model with the Penn State–NCAR MM5 modeling system. Part I: Model implementation and sensitivity. *Mon. Wea. Rev.,* **129,** 569–585.

Clark, A. J., and Coauthors, 2012: An overview of the 2010 Hazardous Weather Testbed Experimental Forecast Program Spring Program. *Bull. Amer. Meteor. Soc.,* **93,** 55–74.

Coniglio, M. C., and D. J. Stensrud, 2001: Simulation of a progressive derecho using composite initial conditions. *Mon. Wea. Rev.,* **129,** 1593–1616.

——, and ——, 2004: Interpreting the climatology of derechoes. *Wea. Forecasting,* **19,** 595–605.

——, K. L. Elmore, J. S. Kain, S. J. Weiss, M. Xue, and M. L. Weisman, 2010: Evaluation of WRF model output for severe weather forecasting from the 2008 NOAA Hazardous Weather Testbed Spring Experiment. *Wea. Forecasting,* **25,** 408–427.

——, S. F. Corfidi, and J. S. Kain, 2011: Environment and early evolution of the 8 May 2009 derecho-producing convective system. *Mon. Wea. Rev.,* **139,** 1083–1102.

——, ——, and ——, 2012: Views on applying RKW theory: An illustration using the 8 May 2009 derecho-producing convective system. *Mon. Wea. Rev.,* **140,** 1023–1043.

Cram, T. A., M. T. Montgomery, and R. F. A. Hertenstein, 2002: Early evolution of vertical vorticity in a numerically simulated idealized convective line. *J. Atmos. Sci.,* **59,** 2113–2127.

Davies-Jones, R. P., 1984: Streamwise vorticity: The origin of updraft rotation in supercell storms. *J. Atmos. Sci.,* **41,** 2991–3006.

Davis, C. A., and M. L. Weisman, 1994: Balanced dynamics of mesoscale vortices produced in simulated convective systems. *J. Atmos. Sci.,* **51,** 2005–2030.

——, and S. B. Trier, 2002: Cloud-resolving simulations of mesoscale vortex intensification and its effect on a serial mesoscale convective system. *Mon. Wea. Rev.,* **130,** 2839–2858.

——, and ——, 2007: Mesoscale convective vortices observed during BAMEX. Part I: Kinematic and thermodynamic structure. *Mon. Wea. Rev.,* **135,** 2029–2049.

——, and T. J. Galarneau, 2009: The vertical structure of mesoscale convective vortices. *J. Atmos. Sci.,* **66,** 686–704.

Done, J., C. A. Davis, and M. L. Weisman, 2004: The next generation of NWP: Explicit forecasts of convection using the Weather Research and Forecast (WRF) model. *Atmos. Sci. Lett.,* **5,** 110–117, doi:10.1002/asl.72.

Doswell, C. A., III, A. R. Moller, and R. Przybylinski, 1990: A unified set of conceptual models for variations on the supercell theme. Preprints, *16th Conf. on Severe Local Storms,* Kananaskis Park, AB, Canada, Amer. Meteor. Soc., 40–45.

Dudhia, J., 1989: Numerical study of convection observed during the Winter Monsoon Experiment using a mesoscale two-dimensional model. *J. Atmos. Sci.,* **46,** 3077–3107.

Engerer, N. A., D. J. Stensrud, and M. C. Coniglio, 2008: Surface characteristics of observed cold pools. *Mon. Wea. Rev.,* **136,** 4839–4849.

Evans, J. S., 1998: An examination of observed shear profiles associated with long-lived bow echoes. Preprints, *19th Conf. on Severe Local Storms,* Minneapolis, MN, Amer. Meteor. Soc., 30–33.

——, and C. A. Doswell III, 2001: Examination of derecho environments using proximity soundings. *Wea. Forecasting,* **16,** 329–342.

Fritsch, J. M., J. D. Murphy, and J. S. Kain, 1994: Warm core vortex amplification over land. *J. Atmos. Sci.,* **51,** 1780–1807.

Fujita, T. T., 1978: Manual of downburst identification for Project Nimrod. Satellite and Mesometeorology Research Paper 156, Dept. of Geophysical Sciences, University of Chicago, 104 pp.

Funk, T. W., K. E. Darmofal, J. D. Kirkpatrick, V. L. Dewald, R. W. Przybylinski, G. K. Schmocker, and Y.-J. Lin, 1999: Storm reflectivity and mesocyclone evolution associated with the 15 April 1994 squall line over Kentucky and southern Indiana. *Wea. Forecasting,* **14,** 976–993.

Hendricks, E. A., M. T. Montgomery, and C. A. Davis, 2004: The role of vortical hot towers in the formation of Tropical Cyclone Diana (1984). *J. Atmos. Sci.,* **61,** 1209–1232.

Hong, S., and J. J. Lim, 2006: The WRF single-moment 6-class microphysics scheme (WSM6). *J. Korean Meteor. Soc.,* **42,** 129–151.

——, Y. Noh, and J. Dudhia, 2006: A new vertical diffusion package with an explicit treatment of entrainment processes. *Mon. Wea. Rev.,* **134,** 2318–2341.

Houze, R. A., Jr., S. A. Rutledge, M. I. Biggerstaff, and B. F. Smull, 1989: Interpretation of Doppler weather radar displays of midlatitude mesoscale convective systems. *Bull. Amer. Meteor. Soc.,* **70,** 608–619.

Janjić, Z. I., 2001: Nonsingular implementation of the Mellor–Yamada level 2.5 scheme in the NCEP Meso Model. NOAA/NWS/NCEP Office Note 437, 61 pp.

Johns, R. H., and W. D. Hirt, 1987: Derechos: Widespread convectively induced windstorms. *Wea. Forecasting,* **2,** 32–49.

Johnson, R. H., and P. J. Hamilton, 1988: The relationship of surface pressure features to the precipitation and airflow structure of an intense midlatitude squall line. *Mon. Wea. Rev.,* **116,** 1444–1473.

Kain, J. S., S. J. Weiss, M. E. Baldwin, G. W. Carbin, D. A. Bright, J. J. Levit, and J. A. Hart, 2005: Evaluating high-resolution configurations of the WRF model that are used to forecast severe convective weather: The 2005 SPC/NSSL Spring Program. Preprints, *21st Conf. on Weather Analysis and Forecasting/17th Conf. on Numerical Weather Prediction,* Washington, DC, Amer. Meteor. Soc., 2A.5. [Available online at https://ams.confex.com/ams/pdfpapers/94843.pdf.]

——, ——, J. J. Levit, M. E. Baldwin, and D. R. Bright, 2006: Examination of convective allowing configurations of the WRF model for the prediction of severe convective weather: The SPC/NSSL Spring Program 2004. *Wea. Forecasting,* **21,** 167–181.

——, and Coauthors, 2008: Some practical considerations regarding horizontal resolution in the first generation of operational convection-allowing NWP *Wea. Forecasting,* **23,** 931–952.

Loehrer, S. M., and R. H. Johnson, 1995: Surface pressure and precipitation life cycle characteristics of PRE-STORM mesoscale convective systems. *Mon. Wea. Rev.,* **123,** 600–621.

Maddox, R. A., 1980: Mesoscale convective complexes. *Bull. Amer. Meteor. Soc.,* **61,** 1374–1387.

Menard, R. D., and J. M. Fritsch, 1989: A mesoscale convective complex-generated inertially stable warm core vortex. *Mon. Wea. Rev.,* **117,** 1237–1260.

Mlawer, E. J., S. J. Taubman, P. D. Brown, M. J. Iacono, and S. A. Clough, 1997: Radiative transfer for inhomogeneous atmosphere: RRTM, a validated correlated-k model for the longwave. *J. Geophys. Res.,* **102** (D14), 16 663–16 682.

Moller, A. R., C. A. Doswell, and R. Przybylinski, 1990: High-precipitation supercells: A conceptual model and documentation. Preprints, *16th Conf. on Severe Local Storms,* Kananaskis Park, AB, Canada, Amer. Meteor. Soc., 52–57.

Montgomery, M. T., and B. F. Farrell, 1993: Tropical cyclone formation. *J. Atmos. Sci.,* **50,** 285–310.

Parker, M. D., 2008: Response of simulated squall lines to low-level cooling. *J. Atmos. Sci.,* **65,** 1323–1341.

Pfost, R. L., and A. E. Gerard, 1997: ''Bookend vortex'' induced tornadoes along the Natchez Trace. *Wea. Forecasting,* **12,** 572–580.

Przybylinski, R. W., 1995: The bow echo: Observations, numerical simulations, and severe weather detection methods. *Wea. Forecasting,* **10,** 203–218.

——, and G. K. Schmocker, 1993: The evolution of a widespread convective wind storm event over central and eastern Missouri. Preprints, *13th Conf. on Weather Analysis and Forecasting,* Vienna, VA, Amer. Meteor. Soc., 461–465.

Raymond, D. J., and H. Jiang, 1990: A theory for long-lived mesoscale convective systems. *J. Atmos. Sci.,* **47,** 3067–3077.

Rodgers, R. F., and J. M. Fritsch, 2001: Surface cyclogenesis from convectively driven amplification of midlevel mesoscale convective vortices. *Mon. Wea. Rev.,* **129,** 605–637.

Roth, D., cited 2003: MCS with eye July 21, 2003. NOAA/NCEP/NPC. [Available online at http://www.hpc.ncep.noaa.gov/research/roth/landcane.html.]

Rotunno, R., J. B. Klemp, and M. L. Weisman, 1988: A theory for strong, long-lived squall lines. *J. Atmos. Sci.,* **45,** 463–485.

Schultz, D. M., and G. Vaughan, 2011: Occluded fronts and the occlusion process: A fresh look at conventional wisdom. *Bull. Amer. Meteor. Soc.,* **92,** 443–466.

Shapiro, M. A., and D. Keyser, 1990: Fronts, jet streams and the tropopause. *Extratropical Cyclones: The Erik Palmen Memorial Volume,* C. W. Newton and E. O. Holopainen, Eds., Amer. Meteor. Soc., 167–191.

Sieveking, J. E., and R. W. Przybylinski, 2004: The interaction of a HP supercell thunderstorm and bow echo to produce a prolonged severe wind event in east central Missouri. Preprints, *22nd Conf. on Severe Local Storms,* Hyannis, MA, Amer. Meteor. Soc., 7A.5. [Available online at https://ams.confex.com/ams/pdfpapers/81818.pdf.]

Skamarock, W. C., and J. B. Klemp, 2008: A time-split nonhydrostatic atmospheric model for weather research and forecasting applications. *J. Comput. Phys.,* **227,** 3465–3485.

——, and M. L. Weisman, 2009: The impact of positive-definite moisture transport on NWP precipitation forecasts. *Mon. Wea. Rev.,* **137,** 488–494.

——, ——, and J. B. Klemp, 1994: Three-dimensional evolution of simulated long-lived squall lines. *J. Atmos. Sci.,* **51,** 2563–2584.

——, and Coauthors, 2008: A description of the Advanced Research WRF version 3. NCAR Tech. Note NCAR/TN-475+STR, 113 pp. [Available online at http://www.mmm.ucar.edu/wrf/users/docs/arw_v3.pdf.]

Thompson, G., P. R. Field, W. D. Hall, and R. M. Rasmussen, 2006: A new bulk microphysical parameterization for WRF. *Seventh WRF Users' Workshop,* Boulder, Colorado, NCAR, 5.3. [Available online at http://www.mmm.ucar.edu/wrf/users/workshops/WS2006/WorkshopPapers.htm.]

Trapp, R. T., and M. L. Weisman, 2003: Low-level mesovortices within squall lines and bow echoes. Part II: Their genesis and implications. *Mon. Wea. Rev.,* **131,** 2804–2823.

Trier, S. B., and C. A. Davis, 2007: Mesoscale convective vortices observed during BAMEX. Part II: Influences on secondary deep convection. *Mon. Wea. Rev.,* **135,** 2051–2075.

——, ——, D. A. Ahijevych, M. L. Weisman, and G. H. Bryan, 2006: Mechanisms supporting long-lived episodes of propagating nocturnal convection within a 7-day WRF model simulation. *J. Atmos. Sci.,* **63,** 2437–2461.

Wakimoto, R. M., H. V. Murphy, A. Nester, D. P. Jorgensen, and N. T. Atkins, 2006a: High winds generated by bow echoes. Part I: Overview of the Omaha bow echo 5 July 2003 storm during BAMEX. *Mon. Wea. Rev.,* **134,** 2793–2812.

——, ——, C. A. Davis, and N. T. Atkins, 2006b: High winds generated by bow echoes. Part II: The relationship between the mesovortices and damaging straight-line winds. *Mon. Wea. Rev.,* **134,** 2813–2829.

Weisman, M. L., 1992: The role of convectively generated rear-inflow jets in the evolution of long-lived mesoconvective systems. *J. Atmos. Sci.,* **49,** 1826–1847.

——, 1993: The genesis of severe, long-lived bow echoes. *J. Atmos. Sci.,* **50,** 645–670.

——, and J. B. Klemp, 1984: The structure and classification of numerically simulated convective storms in directionally varying wind shears. *Mon. Wea. Rev.,* **112,** 2479–2498.

——, and C. A. Davis, 1998: Mechanisms for the generation of mesoscale vortices within quasi-linear convective systems. *J. Atmos. Sci.,* **55,** 2603–2622.

——, and R. Rotunno, 2000: The use of vertical wind shear versus helicity in interpreting supercell dynamics. *J. Atmos. Sci.,* **57,** 1452–1472.

——, and R. T. Trapp, 2003: Low-level mesovortices within squall lines and bow echoes. Part I: Overview and environmental shear sensitivities. *Mon. Wea. Rev.,* **131,** 2779–2803.

——, and R. Rotunno, 2004: A theory for strong long-lived squall lines revisited. *J. Atmos. Sci.,* **61,** 361–382.

——, J. B. Klemp, and R. Rotunno, 1988: The structure and evolution of numerically simulated squall lines. *J. Atmos. Sci.,* **45,** 1990–2013.

——, C. A. Davis, W. Wang, K. W. Manning, and J. B. Klemp, 2008: Experiences with 0–36-h explicit convective forecasts with the WRF-ARW model. *Wea. Forecasting,* **23,** 407–437.

Weiss, S. J., J. S. Kain, J. J. Levit, M. E. Baldwin, and D. R. Bright, 2004: Examination of several different versions of the Weather Research and Forecasting (WRF) model for the prediction of severe convective weather: The SPC/NSSL Spring Program 2004. Preprints, *22nd Conf. on Severe Local Storms,* Hyannis, MA, Amer. Meteor. Soc., 17.1. [Available online at https://ams.confex.com/ams/pdfpapers/82052.pdf.]

Wheatley, D. M., and R. J. Trapp, 2008: The effect of mesoscale heterogeneity on the genesis and structure of mesovortices within quasi-linear convective systems. *Mon. Wea. Rev.,* **136,** 4220–4241.

——, ——, and N. T. Atkins, 2006: Radar and damage analysis of severe bow echoes observed during BAMEX. *Mon. Wea. Rev.,* **134,** 791–806.

Wolf, P. L., 1998: WSR-88D radar depiction of supercell–bow-echo interaction: Unexpected evolution of a large, tornadic, comma-shaped supercell over eastern Oklahoma. *Wea. Forecasting,* **13,** 492–504.